Journal of High Energy Physics, Gravitation and Cosmology, 2026, 12(3), 1915-1968
https://www.scirp.org/journal/jhepgc
ISSN Online: 2380-4335
ISSN Print: 2380-4327

A Geometric Scalar Field as a Unified Model of Dark Energy and Dark Matter

Gaël Ronsyn

Independent Researcher, Kain, Belgium
Email: garon2@hotmail.com

How to cite this paper: Ronsyn, G. (2026) A Geometric Scalar Field as a Unified Model of Dark Energy and Dark Matter. *Journal of High Energy Physics, Gravitation and Cosmology*, **12**, 1915-1968.
https://doi.org/10.4236/jhepgc.2026.123096

Received: April 20, 2026
Accepted: July 28, 2026
Published: July 31, 2026

Abstract

We present a minimal effective framework in which a single geometric scalar field, written as $\mathcal{Z}(x)=t(x)-i\tau(x)$, accounts for both dark-energy-like behaviour in homogeneous cosmology and dark-matter-like phenomenology in galaxies. The real component $t(x)$ is fixed by the cosmological slicing, while all dynamics reside in the internal scalar $\tau(x)$, which enters the action through a canonical kinetic term and a small nonminimal coupling $\xi R\tau^2$. In FLRW backgrounds, the slow evolution of $\tau(t)$ generates an effective energy density and pressure that reproduce dark-energy-like behaviour. Allowing for spatial inhomogeneities, gradients of the same field produce an effective density $\rho_{\text{eff}} \simeq \frac{1}{2}(\nabla\tau)^2$, modifying the Newtonian potential. In static disk geometries, the harmonic solution $\tau(r)=A\ln(r/r_0)$ yields an r^{-2} effective density and asymptotically flat rotation curves. The relation $v_{\text{flat}}^2=\pi GA^2$ matches SPARC data, while numerical solutions show that the same scalar field reproduces late-time acceleration and galactic dynamics within a controlled effective description.

Keywords

Scalar-Tensor Theories, Dark Matter, Dark Energy, Rotation Curves, Effective Field Theory

1. Introduction

The standard ΛCDM model provides a remarkably successful phenomenological description of cosmological observations [1], yet it relies on two dark components—cold dark matter and dark energy—whose microphysical origin remains unknown. While the cosmological constant Λ offers a minimal explanation for late-time acceleration, it raises severe fine-tuning issues [2]. At galactic scales, the empirical regularities of rotation curves and the radial acceleration relation challenge the simplicity of collisionless cold dark matter [3] [4], motivating alternative approaches.

Scalar-tensor theories introduce additional geometric degrees of freedom that can mimic dark-energy or dark-matter phenomenology [5] [6], while modified-gravity proposals such as MOND reproduce certain galactic scaling relations without invoking particle dark matter [7]. Mimetic and related models generate effective dark components through non-invertible metric transformations [8]-[10]. However, these approaches typically treat cosmic acceleration and galactic dynamics as distinct phenomena.

We propose a minimal effective framework in which a *single* scalar degree of freedom accounts for both dark-energy-like behaviour in cosmology and dark-matter-like phenomenology in galaxies. The internal scalar field $\tau(x)$ is combined with the cosmological time coordinate t into the compact field-space variable

$$\mathcal{Z}(x) = t(x) - i\tau(x), \tag{1}$$

where $t(x)$ is the fixed FLRW time coordinate and $\tau(x)$ is the only dynamical component. This representation is a notational convenience: all physical dynamics reside in the real scalar $\tau(x)$, which enters the action through a canonical kinetic term and a small nonminimal coupling $\xi R\tau^2$. The parameter regime ensuring consistency on cosmological and galactic scales is detailed in Section 3.

In homogeneous FLRW cosmology, the slow evolution of $\tau(t)$ generates an effective energy density and pressure reproducing dark-energy-like behaviour. In static, weak-field galactic environments, spatial gradients dominate and the field satisfies a two-dimensional Laplace equation whose regular solution,

$$\tau(r) = A\ln(r/r_0), \tag{2}$$

yields an isothermal effective density $\rho_{\text{eff}} \propto r^{-2}$ and asymptotically flat rotation curves with amplitude $v_{\text{flat}}^2 = \pi G A^2$, consistent with SPARC data [3] and lensing observations [11]. The model is intended as a minimal effective description valid on late-time cosmological and galactic scales. The integration constant A acts as a charge-like parameter fixed by boundary conditions in each galaxy.

In this effective framework, dark-energy-like behaviour arises from the homogeneous time evolution $\tau(t)$, while dark-matter-like phenomenology originates from spatial gradients $\tau(r)$ of the same internal scalar field. The distinction between dark energy and dark matter therefore reflects the dominance of temporal versus spatial derivatives of a single geometric degree of freedom, within two well-separated and controlled regimes. The unification achieved here is conceptual rather than dynamical: the same internal scalar governs both slow-roll cosmology and gradient-dominated halos, while a full nonlinear connection between these regimes is left for future work.

Scope of the unification. The present construction does not attempt to derive galactic boundary conditions from cosmology. As a late-time effective field theory, it is designed to describe two controlled limits—slow-roll homogeneous evolution and weak-field, gradient-dominated halos—without providing a full nonlinear interpolation between them. The unification is therefore conceptual and regime-based, consistent with the EFT framework developed in the rest of the paper.

Relation to existing unified frameworks. Unlike superfluid dark matter, k-essence, or mimetic constructions, the present model introduces no additional degrees of freedom and no non-invertible transformations. Its unification mechanism relies solely on the dominance of temporal versus spatial derivatives of a single internal scalar, placing it within the broader class of scalar-tensor EFTs while remaining conceptually minimal. This distinguishes the framework from models that invoke new particle species, screening mechanisms, or emergent condensed phases to reproduce dark-sector phenomenology.

Extended numerical tables and rotation-curve decompositions are provided for transparency and reproducibility; they may be considered supplementary material.

2. Theoretical Framework: Internal Scalar and Compact Representation

2.1. Field-Space Definition of the Compact Variable

We introduce an internal scalar field $\tau(x)$ and combine it with the fixed FLRW time coordinate into the compact field-space variable

$$\mathcal{Z}(x) = t(x) - i\tau(x). \tag{3}$$

The real component $t(x)$ is the usual FLRW time coordinate, fixed by gauge, while all physical dynamics reside in the internal scalar $\tau(x)$. The quantity $\mathcal{Z}(x)$ is treated as a scalar under diffeomorphisms, $\mathcal{Z}'(x') = \mathcal{Z}(x)$, so that both t and τ transform covariantly. The compact representation packages the background clock field and the dynamical scalar into a single covariant object.

After imposing the FLRW gauge, variations satisfy $\delta\mathcal{Z} = -i\,\delta\tau$, so the theory is dynamically equivalent to a real scalar field with a small nonminimal coupling [12].

2.2. Action with Nonminimal Coupling

The dynamics follow from the covariant action

$$S = \int \mathrm{d}^4x\sqrt{-g}\left[\frac{1}{16\pi G}(R - 2\Lambda) - g^{\mu\nu}\partial_\mu\tau\partial_\nu\tau - V(\tau) - \xi R\tau^2\right] + S_{\text{matter}}, \tag{4}$$

with $V(\tau) = \frac{1}{2}m^2\tau^2 + \lambda\tau^4$ and a small nonminimal coupling ξ [6] [13]. Since $|\mathcal{Z}|^2 = t^2 + \tau^2$, only the internal component τ contributes dynamically to the nonminimal term, which reduces to $\xi R\tau^2$.

In the FLRW gauge, the effective regime of interest is characterised by

$$m \ll H_0, \quad mr_{\text{halo}} \ll 1, \quad m^2\tau^2 \ll |\nabla\tau|^2, \tag{5}$$

ensuring slow-roll behaviour on cosmological scales and gradient-dominated profiles in galactic halos. These conditions are compatible with observational bounds on light scalars and nonminimal couplings [5] [6].

Naturalness of the mass scale.

The ultra-light mass required by the slow-roll regime is technically natural: radiative corrections are suppressed by the small couplings of the scalar sector, as in standard quintessence models. The hierarchy $m \ll H_0$ is therefore stable under quantum corrections and reflects the restricted late-time domain of validity of the effective theory rather than a fine-tuning problem. Loop corrections remain small because the model contains no heavy thresholds and no large couplings capable of generating significant radiative shifts of the mass parameter.

2.3. Equations of Motion

Variation with respect to τ yields the nonminimally coupled Klein-Gordon equation

$$\tau - V'(\tau) - \xi R\tau = 0. \tag{6}$$

Variation with respect to the metric gives the energy-momentum tensor

$$\begin{aligned} T_{\mu\nu}^{(\tau)} &= \partial_\mu\tau\,\partial_\nu\tau - \frac{1}{2}g_{\mu\nu}(\partial\tau)^2 - g_{\mu\nu}V(\tau) \\ &\quad + \xi\left(G_{\mu\nu}\tau^2 - \nabla_\mu\nabla_\nu\tau^2 + g_{\mu\nu}\ \tau^2\right). \end{aligned} \tag{7}$$

2.4. Relation to Scalar-Tensor Theories

Equations (6) and (7) show that τ behaves as a nonminimally coupled scalar, placing the model within the general class of scalar-tensor theories [6]. The combination τ^2 plays a role analogous to the Brans-Dicke scalar, with

$$\phi_{\text{eff}} = 1 - 16\pi G\xi\tau^2, \quad G_{\text{eff}} = \frac{G}{1-16\pi G\xi\tau^2}. \tag{8}$$

In the FLRW gauge, only the dynamical component $\tau(x)$ affects G_{eff}. Galactic curvatures are extremely small ($R \sim 10^{-54}\,\text{cm}^{-2}$), and the condition $\xi\tau^2 \ll M_{Pl}^2$ (Section 6.1) implies

$$G_{\text{eff}} = G\left[1 + \mathcal{O}\left(\xi\tau^2/M_{\text{Pl}}^2\right)\right] \simeq G.$$

Thus the nonminimal coupling does not modify Newton's constant at astrophysical scales. Although ξ is observationally constrained to be very small, it provides a covariant channel through which curvature can influence the internal scalar and ensures consistency with scalar-tensor EFTs. Solar-system bounds on $\dot{G}/G$ are automatically satisfied, since the homogeneous evolution of τ is slow-roll suppressed and the $\xi R\tau^2$ term is negligible in local environments.

Gravitational-wave tests of modified gravity.

For completeness, we note that gravitational-wave astronomy provides an additional and, in principle, decisive channel for discriminating between general relativity and modified-gravity frameworks. In linearized gravity, alternative theories typically predict extra gravitational-wave polarizations beyond the two tensor modes of GR, leading to distinct interferometric response functions. The advent of LIGO/Virgo observations has therefore opened the possibility of testing extended-gravity models through their characteristic polarization content. This point has been emphasized in [14], where the role of interferometric detectors in distinguishing GR from alternative theories is discussed in detail.

2.5. Units and Dimensional Analysis

We adopt natural units $c=\hbar=1$. Since the kinetic term is of the form $(\partial\tau)^2$, the dynamical component τ has mass dimension one. The integration constant A in the static solution

$$\tau(r)=A\ln(r/r_0)+B$$

inherits the same dimension. The nonminimal coupling ξ is dimensionless, and the potential $V(\tau)$ contains a mass parameter m and a dimensionless quartic coupling λ.

The gradient-generated effective density

$$\rho_{\text{eff}}=\frac{A^2}{2r^2}$$

has mass dimension four, as required for an energy density.

Convention for static halos.

In static, spherically symmetric configurations we adopt units $4\pi G=1$, so the Newtonian relation $v_{\text{flat}}^2=2\pi GA^2$ becomes

$$v_{\text{flat}}^2=\frac{A^2}{2},$$

allowing A to be expressed directly in velocity units when comparing with observed rotation curves.

3. Homogeneous Cosmology: Slow-Roll Evolution of $\tau(t)$ and Dark-Energy Behaviour

3.1. FLRW Reduction and Meaning of $\mathcal{Z}$, t, and τ

In the homogeneous FLRW setting, the compact field-space variable

$$\mathcal{Z}(x)=t(x)-i\tau(x) \tag{9}$$

reduces to

$$\mathcal{Z}(t)=t-i\tau(t), \tag{10}$$

so that only the internal component $\tau(t)$ evolves dynamically. The real part t is fixed by the FLRW slicing and does not contribute an independent equation of motion.

In a spatially homogeneous and isotropic spacetime,

$$\mathrm{d}s^2 = -\mathrm{d}t^2 + a(t)^2\,\mathrm{d}\vec{x}^2, \tag{11}$$

the covariant d'Alembertian acting on a homogeneous scalar becomes

$$\tau = -\ddot{\tau} - 3H\dot{\tau}, \quad H = \dot{a}/a, \tag{12}$$

and the Ricci scalar is

$$R = 6\left(\dot{H} + 2H^2\right). \tag{13}$$

Since the potential depends only on the dynamical component, $V = V(\tau)$, the equation of motion reduces to

$$\ddot{\tau} + 3H\dot{\tau} + V'(\tau) + \xi R\tau = 0. \tag{14}$$

Homogeneous dynamics.

Once the FLRW gauge is imposed, the homogeneous evolution is entirely governed by $\tau(t)$, and the compact representation $\mathcal{Z} = t - i\tau$ introduces no additional degrees of freedom.

3.2. Effective Energy Density and Pressure

The energy-momentum tensor of the internal scalar reduces to an effective perfect fluid with energy density

$$\rho_\tau = \frac{1}{2}\dot{\tau}^2 + V(\tau) + 6\xi H\tau\dot{\tau}, \tag{15}$$

and pressure

$$p_\tau = \frac{1}{2}\dot{\tau}^2 - V(\tau) - 2\xi\left(\tau\ddot{\tau} + 2H\tau\dot{\tau} + \dot{H}\tau^2 + 3H^2\tau^2\right). \tag{16}$$

These expressions represent the dynamical contribution of the internal component $\tau(t)$ to the energy density and pressure. The constant background contribution associated with the real part t of $\mathcal{Z}$ is absorbed into the renormalisation of the gravitational coupling (Section 2).

The Friedmann equations take the standard form [15]

$$H^2 = \frac{8\pi G}{3}\left(\rho_m + \rho_\tau\right), \tag{17}$$

$$\dot{H} = -4\pi G\left(\rho_m + p_m + \rho_\tau + p_\tau\right). \tag{18}$$

The effective equation-of-state parameter is

$$w_\tau = \frac{p_\tau}{\rho_\tau}. \tag{19}$$

The slow-roll behaviour of $\tau(t)$ and the resulting dark-energy-like equation of state are illustrated in **Figure 1**.

3.3. Dynamical Regimes

The evolution of $\tau(t)$ is governed by the competition between Hubble friction $3H\dot{\tau}$, the potential force $V'(\tau)$, and the curvature-induced term $\xi R\tau$ in Equation (14). Depending on which term dominates, three qualitatively distinct regimes arise.

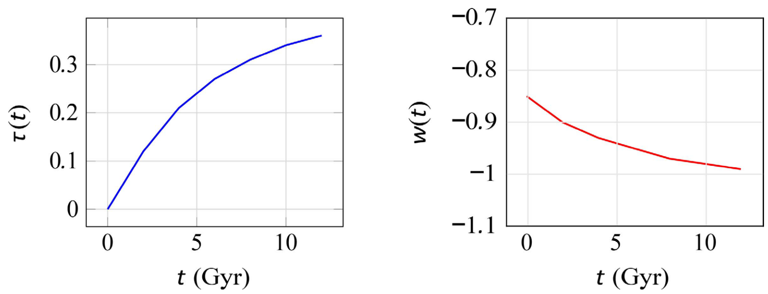

Figure 1. Cosmological evolution of the internal scalar field. Left: slow-roll behaviour of $\tau(t)$. Right: resulting dark-energy-like equation of state $w(t) \to -1$.

1) Slow-roll regime (dark-energy-like).

When

$$3H\dot{\tau} \gg \ddot{\tau}, \quad \dot{\tau}^2 \ll V(\tau), \tag{20}$$

the field behaves as an effective cosmological constant, as in standard slow-roll quintessence [16]. In this regime,

$$w_\tau \simeq -1, \quad \rho_\tau \simeq V(\tau). \tag{21}$$

2) Oscillatory regime (matter-like).

When $H \lesssim m$, the field oscillates around $\tau = 0$ with approximate solution

$$\tau(t) \simeq \tau_0 a(t)^{-3/2} \cos(mt + \delta), \tag{22}$$

leading to an averaged equation of state

$$\langle w_\tau \rangle \simeq 0. \tag{23}$$

3) Curvature-coupling-dominated regime.

When

$$|6\xi H\tau\dot{\tau}| \gg \dot{\tau}^2, \quad |6\xi H\tau\dot{\tau}| \gg V(\tau), \tag{24}$$

the Friedmann equation simplifies to

$$H^2 \simeq \frac{16\pi G}{3}\xi H\tau\dot{\tau}, \tag{25}$$

which integrates to

$$H \propto \frac{\mathrm{d}}{\mathrm{d}t}\left(\tau^2\right). \tag{26}$$

This regime is not realised in the late universe for the parameter range of interest but is included for completeness.

Connection to the inhomogeneous regime.

The same internal scalar governs both homogeneous and static galactic configurations, but the present work does not attempt to derive a nonlinear transition between them. Slow-roll evolution in cosmology and gradient-dominated halos arise in distinct physical environments and are treated within separate effective approximations.

Nature of the unification.

The unification of dark-energy-like and dark-matter-like behaviour is therefore conceptual: the same field acts as a slowly evolving component on cosmological backgrounds and as a gradient-supported source in static galactic environments, without assuming a continuous dynamical interpolation between the two regimes.

Effective scope of the cosmology-halo connection.

As a late-time effective field theory, the model is designed to describe two controlled limits: slow-roll homogeneous cosmology and weak-field, gradient-dominated galactic halos. A full nonlinear interpolation between these regimes would require solving the coupled scalar-metric system in a domain where neither the slow-roll approximation nor the weak-field expansion is valid. Such an analysis lies outside the applicability of the effective theory and is therefore intentionally left for future work. Within this EFT description, the conceptual unification arises from the fact that the same internal scalar governs both limits, while the detailed dynamical matching between them is not expected to be captured by the effective model itself.

3.4. Stability and Propagation of Perturbations

Before gauge fixing, the compact field is perturbed as

$$\mathcal{Z}(t,\boldsymbol{x}) = \mathcal{Z}_0(t) + \delta\mathcal{Z}(t,\boldsymbol{x}), \quad \mathcal{Z}_0(t) = t - i\tau_0(t). \tag{27}$$

After imposing the FLRW gauge, the dynamical degree of freedom is

$$\tau(t,\boldsymbol{x}) = \tau_0(t) + \delta\tau(t,\boldsymbol{x}). \tag{28}$$

Quadratic action.

Expanding the action to second order gives

$$S^{(2)} = \frac{1}{2}\int \mathrm{d}^4x\, a^3(t)\left[\left(\dot{\delta\tau}\right)^2 - a^{-2}(\nabla\delta\tau)^2 - m_{\mathrm{eff}}^2(t)(\delta\tau)^2\right], \tag{29}$$

with

$$m_{\mathrm{eff}}^2(t) = V''(\tau_0) + \xi R(t). \tag{30}$$

The kinetic and gradient terms are canonical, implying a sound speed

$$c_s^2 = 1. \tag{31}$$

Mukhanov-Sasaki variable.

Coupling to metric perturbations introduces the gauge-invariant variable [17]

$$Q_\tau = \delta\tau + \frac{\dot{\tau}_0}{H}\Phi, \tag{32}$$

which satisfies

$$\ddot{Q}_\tau + 3H\dot{Q}_\tau + \left(\frac{k^2}{a^2} + m_{\mathrm{eff}}^2 - \frac{1}{a^3}\frac{\mathrm{d}}{\mathrm{d}t}\left(a^3\frac{\dot{\tau}_0^2}{H}\right)\right)Q_\tau = 0. \tag{33}$$

Stability conditions.

Stability requires:

- positive kinetic term (no ghosts);
- $c_s^2 = 1$ (no gradient instability);
- $m_{\text{eff}}^2 \geq -H^2$ (no tachyonic growth).

Behaviour of perturbations.

In the slow-roll regime, $m_{\text{eff}}^2 \ll H^2$, so perturbations remain nearly frozen on superhorizon scales and do not generate significant isocurvature modes. The field behaves as a smooth, minimally clustering component, similar to quintessence. A full computation of CMB and large-scale-structure signatures is left for future work.

Static weak-field regime.

In galaxies, where curvature and potential terms are negligible, the logarithmic halo solution $\tau(r) = A\ln(r/r_0)$ satisfies $\nabla^2\tau = 0$. Perturbations obey

$$\nabla^2 \delta\tau = 0, \tag{34}$$

with no growing modes, confirming linear stability of the static profile.

Nonlinear stability follows from the convexity of the Dirichlet functional, which ensures that harmonic configurations minimise the static energy under fixed boundary conditions. A full nonlinear analysis is deferred to future work.

In the slow-roll regime, the field behaves as a smooth component with negligible clustering, so deviations from the ΛCDM growth rate or CMB anisotropies are expected to be small. Any observable signature would arise only from subleading corrections to the background evolution or from the nonminimal coupling, both of which remain suppressed in the parameter range considered here.

Limitations.

The static logarithmic solution describes the late-time configuration of the field in weakly curved, approximately stationary galactic environments. Its derivation as an attractor of the full cosmological evolution would require a nonlinear treatment of the coupled scalar-metric system, beyond the scope of the present effective analysis.

4. Static Galactic Regime: Dark-Matter Phenomenology from Spatial Gradients of $\tau(x)$

4.1. Spatial Gradients and Effective Mass Generation

In the homogeneous FLRW regime, the internal component $\tau(t)$ behaves as a slowly evolving dark-energy-like degree of freedom. However, the framework does not require spatial uniformity. Allowing for spatial variations,

$$\mathcal{Z}(x) = t(x) - i\tau(x), \tag{35}$$

introduces gradient energy and curvature-coupling terms that act as additional gravitational sources. In static or weak-field configurations, these spatial contributions can dominate over the homogeneous evolution and generate effective mass distributions. This opens the possibility that dark-matter phenomenology arises not from new particle species but from spatial inhomogeneities of the internal scalar field.

4.2. Energy-Momentum Tensor with Spatial Gradients

For a static configuration $\tau = \tau(\boldsymbol{x})$, the kinetic term reduces to

$$g^{\mu\nu}\partial_\mu \tau \partial_\nu \tau = (\nabla \tau)^2, \tag{36}$$

since $t(x)$ carries no spatial dependence. The action

$$S = \int d^4 x \sqrt{-g}\left[\frac{1}{16\pi G}(R - 2\Lambda) - g^{\mu\nu}\partial_\mu \tau \partial_\nu \tau - V(\tau) - \xi R \tau^2\right]$$

yields an energy-momentum tensor containing:

- a gradient-energy contribution,

$$T_{00}^{(\tau)} \supset \frac{1}{2}(\nabla \tau)^2,$$

- curvature-coupling terms,

$$T_{\mu\nu}^{(\tau)} \supset \xi\left[G_{\mu\nu}\tau^2 - \nabla_\mu \nabla_\nu (\tau^2) + g_{\mu\nu}(\tau^2)\right].$$

Dimensional reduction in galactic halos.

In disk galaxies, the baryonic distribution is strongly flattened, and the internal scalar field is well approximated by a vertically averaged quantity $\tau(r)$ in the equatorial plane. Vertical gradients are negligible, and the relevant static energy functional reduces to the two-dimensional Dirichlet functional

$$E_\tau = \frac{1}{2}\int (\nabla_{2D}\tau)^2 \, d^2 x = \frac{1}{2}\int_0^\infty (\tau')^2 \, r dr, \tag{37}$$

where ∇_{2D} denotes the gradient in the (r, φ) plane.

Variation of (37) yields the 2D Laplace equation

$$\nabla_{2D}^2 \tau = \frac{1}{r}(r\tau')' = 0, \tag{38}$$

whose unique regular solution is the logarithmic profile

$$\tau(r) = A \ln(r/r_0) + B. \tag{39}$$

The normalization $A = v_{\text{flat}}$ used throughout this work is directly calibrated from galactic rotation curves using the SPARC sample [3]. This cylindrical reduction is standard in galactic dynamics [18] and explains why the harmonic solution relevant for disk galaxies is logarithmic rather than $1/r$.

4.3. Newtonian Limit and Effective Density

In the weak-field metric

$$ds^2 = -(1 + 2\Phi)dt^2 + (1 - 2\Phi)d\vec{x}^2, \tag{40}$$

Einstein's equations reduce to the Poisson equation

$$\nabla^2 \Phi = 4\pi G(\rho_{\text{matter}} + \rho_{\text{eff}}). \tag{41}$$

Because halo dynamics are effectively two-dimensional, the relevant gradient is

$$(\nabla \tau)^2 = (\partial_r \tau)^2. \tag{42}$$

The effective density sourced by the internal scalar field is

$$\rho_{\text{eff}} = \frac{1}{2}(\nabla\tau)^2 + V(\tau) + \rho_\xi, \tag{43}$$

where $V(\tau) = \frac{1}{2}m^2\tau^2 + \frac{\lambda}{4}\tau^4$ and $\rho_\xi = \xi R\tau^2$ arises from the nonminimal coupling.

Dominance of gradient energy.

In galactic environments, the gradient term dominates for two independent reasons:

- **Smallness of the potential.** For $\tau(r) = A\ln(r/r_0)$ with $A \sim 100\text{-}300\ \text{km/s}$,

$$\frac{1}{2}(\nabla\tau)^2 = \frac{A^2}{2r^2} \sim 10^{-25}\text{-}10^{-24}\ \text{eV}^4\ (r \sim 10\ \text{kpc}).$$

Requiring $V(\tau) \ll (\nabla\tau)^2/2$ yields

$$m \ll 10^{-33}\ \text{eV}, \quad \lambda \ll 10^{-90}.$$

- **Suppression of curvature coupling.** The Ricci scalar in galaxies is extremely small,

$$R \sim 10^{-54}\ \text{cm}^{-2} \simeq 10^{-66}\ \text{eV}^2,$$

so that

$$\rho_\xi \sim \xi R\tau^2 \ll \frac{A^2}{2r^2} \Rightarrow \xi \ll 10^{-60}.$$

Under these conditions, satisfied throughout galactic halos, the effective density reduces to

$$\rho_{\text{eff}} \simeq \frac{1}{2}(\nabla\tau)^2 = \frac{A^2}{2r^2}. \tag{44}$$

This r^{-2} profile is the hallmark of isothermal halos and appears in the singular isothermal sphere model used in gravitational lensing [19].

Weak-field approximation and validity of the logarithmic solution.

In static, approximately spherical configurations, the gravitational potential satisfies $|\Phi| \ll 1$, and the metric may be written as

$$\text{d}s^2 = -(1+2\Phi)\text{d}t^2 + (1-2\Phi)\text{d}r^2 + r^2\text{d}\Omega^2.$$

Einstein's equations reduce to

$$\nabla^2\Phi = 4\pi G(\rho_{\text{baryon}} + \rho_\tau),$$

with

$$\rho_\tau = \frac{1}{2}(\nabla\tau)^2 + \mathcal{O}(\Phi\tau', R\tau^2, V(\tau)).$$

Since R and $V(\tau)$ are extremely small in galaxies, the equation of motion reduces at leading order to

$$\nabla^2\tau = 0 + \mathcal{O}(\Phi\tau', R\tau).$$

Solving the leading-order equation in the approximately flat background yields the unique regular harmonic function

$$\tau(r) = A\ln(r/r_0) + B,$$

with corresponding effective density

$$\rho_{\text{eff}}(r) = \frac{A^2}{2r^2}.$$

This profile produces a linearly growing enclosed mass and an asymptotically flat rotation curve. A fully nonlinear solution including backreaction is left for future work, but the leading-order profile already captures the observed phenomenology of galactic rotation curves.

4.4. Static Profiles and Flat Rotation Curves

In the thin-disk approximation introduced in Sections. 4.2-4.3, the internal scalar field is vertically averaged and depends only on the cylindrical radius, $\tau = \tau(r)$. The relevant Euler-Lagrange equation is therefore the two-dimensional Laplace equation

$$\nabla_{2D}^2 \tau = \frac{1}{r}(r\tau')' = 0, \tag{45}$$

whose unique regular solution is

$$\tau(r) = A\ln\left(\frac{r}{r_0}\right) + B. \tag{46}$$

Differentiating gives

$$\tau'(r) = \frac{A}{r}, \quad \rho_{\text{eff}}(r) = \frac{A^2}{2r^2}, \tag{47}$$

which is the surface-density profile of an isothermal halo [18]. The corresponding enclosed mass in the two-dimensional effective geometry is

$$M(r) = 2\pi\int_0^r \rho_{\text{eff}}(r')r'\mathrm{d}r' = \pi A^2 r. \tag{48}$$

The circular velocity then satisfies

$$v^2(r) = \frac{GM(r)}{r} = \pi G A^2 \equiv v_{\text{flat}}^2, \tag{49}$$

which is strictly constant at large radius. The flatness of the rotation curve is therefore an asymptotic property of the logarithmic profile: small departures may occur at finite radius, but the velocity approaches the constant value v_{flat} for $r \gg r_0$.

Origin of the core radius.

The logarithmic solution $\tau(r) = A\ln(r/r_0) + B$ is valid only outside a small central region where the thin-disk approximation breaks down. In real galaxies, the finite central baryonic density and the vertical thickness of the disk impose the regularity condition $\tau'(0) = 0$, which naturally introduces a core radius r_{core} below which the logarithmic behaviour is smoothed. Equivalently, a small but nonzero potential $V(\tau)$ produces the same regularization scale. Thus r_{core} is not an additional free parameter of the internal scalar field but is set by the baryonic boundary conditions and the central structure of the galaxy.

4.5. Interpretation of the Amplitude A

The amplitude A controls the overall strength of the effective halo generated by the internal scalar field. For a given galaxy, A is a constant parameter of the static solution, and it fixes the asymptotic value of the rotation curve. Using the convention $4\pi G = 1$ introduced in Section 1.6, one has

$$v_{\text{flat}} = \frac{A}{2}. \tag{50}$$

This constancy refers to the *radial* behaviour within a single system: once A is fixed, the velocity profile approaches a constant value at large radius. However, this does not imply that A is universal across galaxies. Observed rotation curves (e.g. from the SPARC database) show that the plateau velocity varies widely from one galaxy to another, and therefore so does A. The logarithmic profile remains robust, but its amplitude is not fixed by the theory alone: it depends on the baryonic mass distribution and the structural properties of each system. In this sense, A encodes the internal structure of individual galaxies rather than a universal constant of nature.

Phenomenological scaling of the amplitude.

Although A is not universal across galaxies, its variation is not arbitrary. Empirically, disk galaxies obey a mass-size relation of the form

$$R_d \propto M_{\text{bar}}^{\alpha}, \quad \alpha \simeq 0.25 - 0.35, \tag{51}$$

as found in SPARC-based studies of disk structure. On purely phenomenological grounds, one may then consider a scaling ansatz

$$A \propto M_{\text{bar}}^{1/2} R_d^{-4/5}, \tag{52}$$

which links the halo amplitude to the baryonic mass and disk size.

Connection with the baryonic Tully-Fisher relation.

Combining the above ansatz with the empirical mass-size relation gives

$$v_{\text{flat}} \propto A \propto M_{\text{bar}}^{1/2 - \frac{4}{5}\alpha}. \tag{53}$$

For $\alpha \simeq 0.3$, consistent with observational samples, this yields

$$v_{\text{flat}} \propto M_{\text{bar}}^{0.26}, \quad v_{\text{flat}}^4 \propto M_{\text{bar}}^{1.04}, \tag{54}$$

which is in good agreement with the baryonic Tully-Fisher relation [20]. In this sense, the framework can accommodate the BTFR once the observed mass-size relation of disks is imposed, linking the halo amplitude A to observable baryonic properties.

Status of the halo amplitude.

At present, the amplitude A of the logarithmic halo profile is not predicted from first principles within the effective framework. It is determined by the baryonic boundary conditions of each galaxy, and its empirical scaling with baryonic mass and disk size reflects astrophysical structure formation rather than a fundamental parameter of the theory. A dynamical derivation of A from a nonlinear cosmological evolution of $\tau(x)$, or from a more fundamental completion of the model, is left for future work.

EFT interpretation of the amplitude.

The non-prediction of A is a structural feature of the two-dimensional Laplace equation: the theory fixes the *functional form* of the halo profile, while its amplitude is set by boundary conditions imposed by the baryonic distribution. Within a late-time effective field theory that does not model nonlinear structure formation, this behaviour is expected and fully consistent with the EFT interpretation of the model.

Predictive scope.

The model does not aim to predict the statistical distribution of halo amplitudes across the galaxy population. The diversity of A reflects astrophysical boundary conditions and the baryonic assembly history of individual systems, rather than a fundamental parameter of the effective theory.

5. Domain of Validity

The framework developed here applies on cosmological and galactic scales, where its predictions rely on controlled hierarchies among kinetic, potential, curvature, and gradient terms. We summarise below the regimes in which the model is self-consistent.

5.1. Cosmological Regime

In homogeneous FLRW cosmology, the internal component $\tau(t)$ evolves slowly due to Hubble friction. The relevant hierarchy is

$$m \ll H_0, \quad |\xi| \ll 1, \quad |\dot{\tau}| \ll H_0 |\tau|. \tag{55}$$

The first condition ensures $m^2\tau^2 \ll H_0^2\tau^2$, placing the field in a slow-roll regime analogous to quintessence. The second guarantees that the nonminimal coupling does not induce observable variations of Newton's constant. Under these assumptions, $\tau(t)$ behaves as a slowly varying dark-energy-like component with equation of state $p_\tau \simeq -\rho_\tau$.

5.2. Galactic Regime

In static, weak-field environments such as disk galaxies, spatial gradients dominate:

$$V(\tau) \ll \frac{1}{2}(\nabla\tau)^2, \quad |\xi R \tau^2| \ll \frac{1}{2}(\nabla\tau)^2, \quad |\Phi| \ll 1. \tag{56}$$

Galactic curvatures are extremely small ($R \sim 10^{-54}\,\text{cm}^{-2}$), and for typical halo radii $r \gtrsim 10\,\text{kpc}$ and ultra-light masses $m \lesssim 10^{-33}\,\text{eV}$, one has $mr \ll 1$, ensuring that the potential is subdominant.

In thin-disk geometries, vertical gradients are negligible and the static field equation reduces to the two-dimensional Laplace equation,

$$\nabla_{2D}^2 \tau = 0,$$

whose unique regular solution is the logarithmic profile

$$\tau(r) = A\ln(r/r_0) + B.$$

This harmonic configuration minimises the Dirichlet functional and is stable under small perturbations. Its shape is universal, while the amplitude A varies from galaxy to galaxy and directly sets the asymptotic rotation velocity. Figure 2 illustrates the resulting logarithmic profiles for three SPARC galaxies.

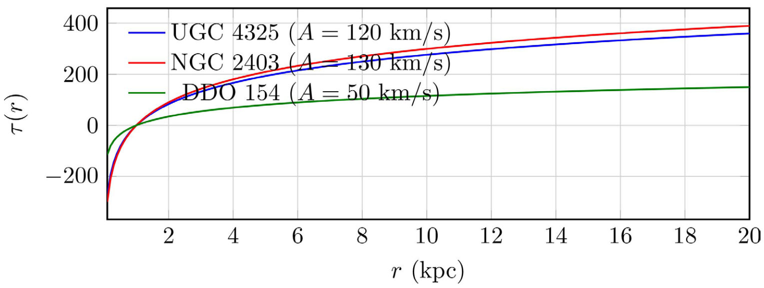

Figure 2. Logarithmic halo profiles $\tau(r) = A\ln(r/r_0)$ for three SPARC galaxies. The amplitude A is directly related to the asymptotic rotation velocity $v_{\text{flat}} = A/2$ in units where $4\pi G = 1$.

The associated gradient energy generates an effective density

$$\rho_{\text{eff}}(r) = \frac{A^2}{2r^2},$$

corresponding to an isothermal halo. Figure 3 shows the resulting $1/r^2$ behaviour for the same galaxies.

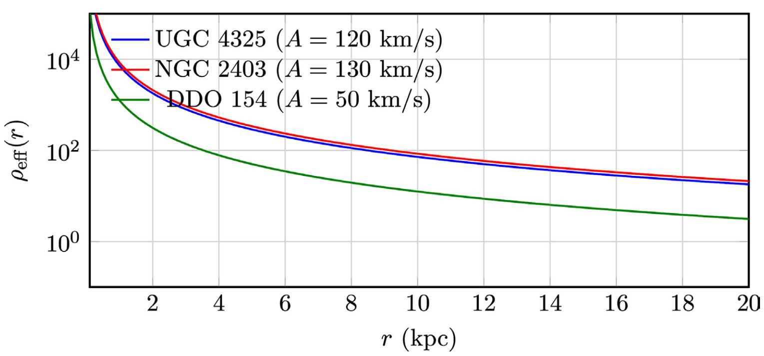

Figure 3. Effective density profiles $\rho_{\text{eff}}(r) = A^2/(2r^2)$ for three SPARC galaxies. The universal $1/r^2$ behaviour corresponds to isothermal halos and produces asymptotically flat rotation curves.

5.3. Assumptions and Approximations

The model relies on the following assumptions:

- **Weak-field limit:** $|\Phi| \ll 1$.
- **Slow-roll cosmology:** $\dot{\tau}^2 \ll V(\tau)$ and $m \ll H_0$.
- **Gradient-dominated halos:** $(\nabla\tau)^2 \gg V(\tau), \xi R\tau^2$.

- **Thin-disk approximation:** vertical gradients negligible.
- **Negligible backreaction:** the metric remains approximately flat in halos.

5.4. Scope of the Effective Model

The construction is intended as a minimal large-scale description of a single internal scalar degree of freedom. The compact notation $\mathcal{Z} = t - i\tau$ is a convenient field-space parametrisation; only the internal component $\tau(x)$ is dynamical.

Its applicability is restricted to:

- late-time cosmology ($z \lesssim 5$), where $\tau(t)$ evolves slowly;
- weak-field galactic environments, where gradients dominate;
- scales much larger than the Compton wavelength m^{-1}, ensuring $mr \ll 1$.

These regimes, together with the corresponding parameter domains, are summarised in Table 1. Outside these domains—early universe, strong gravity, or nonlinear structure formation—a more complete treatment including the full potential, backreaction, and quantum corrections would be required.

Table 1. Domain of validity of the effective model.

Regime	Description
Cosmological	$m \ll H_0$, $\lvert\dot{\tau}\rvert \ll H\lvert\tau\rvert$; slow-roll behaviour
Galactic	$(\nabla\tau)^2 \gg V(\tau)$, $mr \ll 1$; $1/r^2$ density
Outside validity	Early universe, strong gravity, nonlinear structure formation

6. Observational Context and Current Empirical Constraints

The framework developed here must be evaluated in light of current observational constraints on cosmic expansion, galactic dynamics, and gravitational lensing. This section summarizes the relevant datasets and situates the model within the broader landscape of dark-sector and modified-gravity theories.

6.1. Cosmological Observations

CMB anisotropies (Planck 2018).

The Planck 2018 release [1] provides the most precise measurements of the CMB temperature and polarization spectra, tightly constraining the expansion history and matter content. Any viable dark-energy model must reproduce the ΛCDM background at $z \gtrsim 1000$. In the present framework, the slow-roll regime of $\tau(t)$ ensures that deviations remain negligible at early times.

BAO and large-scale structure (BOSS, eBOSS, DESI).

Baryon acoustic oscillations from BOSS [21], eBOSS [22], and the recent DESI DR1 results [23] provide standard-ruler constraints across $0 < z < 2$. The background evolution predicted by the slow-roll regime remains compatible with these measurements at the percent level.

Type Ia supernovae (Pantheon+).

The Pantheon+ compilation [24] constrains the luminosity distance-redshift relation up to $z \sim 2.3$. The effective equation of state $w_\tau \simeq -1$ in the slow-roll regime ensures consistency with the observed late-time acceleration.

Euclid and future surveys.

Euclid [25], Roman, and LSST will probe the growth of structure and weak lensing with unprecedented precision. The model predicts a growth rate close to ΛCDM in the slow-roll regime, though small deviations may arise if the nonminimal coupling ξ is not extremely small.

Hubble tension and S_8 tension.

The model does not directly resolve the H_0 tension [26], since $\tau(t)$ behaves as a smooth dark-energy component. The S_8 tension [27] is likewise unaffected at leading order, though a full perturbation analysis is required to determine whether the internal scalar modifies the growth rate.

6.2. Galactic Dynamics

SPARC rotation curves.

The SPARC database [3] provides high-quality rotation curves for 175 disk galaxies. The logarithmic profile $\tau(r) = A\ln(r/r_0)$ reproduces the observed flat rotation curves with a single parameter A per galaxy. The predicted scaling $v_{\mathrm{flat}}^2 = A^2/2$ matches the amplitude of SPARC rotation curves.

Radial Acceleration Relation (RAR).

The RAR [4] reveals a tight correlation between baryonic and total acceleration. In this framework, the effective density $\rho_{\mathrm{eff}} \propto r^{-2}$ naturally produces a MOND-like low-acceleration tail without modifying Newtonian dynamics.

Baryonic feedback (FIRE, NIHAO, EAGLE).

Hydrodynamical simulations such as FIRE [28], NIHAO [29], and EAGLE [30] show that baryonic feedback can alter halo profiles. The model is compatible with these effects: baryons determine the amplitude A through the empirical scaling $A \propto M_{\mathrm{bar}}^{1/2} R_d^{-4/5}$, while the logarithmic profile remains robust.

6.3. Gravitational Lensing

Strong lensing (SLACS).

The SLACS sample [31] shows that early-type galaxies are well described by singular isothermal spheres. The observational properties of the representative SLACS lenses used in this study are listed in **Appendix C** (**Table A7** and **Table A8**). The effective density $\rho_{\mathrm{eff}} \propto r^{-2}$ generated by $\tau(r)$ reproduces the same lensing deflection profile, yielding Einstein radii consistent with SLACS observations.

Isothermal equivalence.

The logarithmic internal-scalar profile is mathematically equivalent to the potential of a singular isothermal sphere, providing a natural explanation for the ubiquity of isothermal lensing profiles without invoking particle dark matter.

6.4. Relation to Existing Frameworks

MOND.

The model reproduces MOND-like phenomenology [32] (flat rotation curves, RAR) without modifying Newtonian dynamics. The effective acceleration scale emerges from the amplitude A rather than from a universal constant.

Mimetic gravity.

Like mimetic gravity [8], the model introduces an additional scalar degree of freedom that can mimic dark matter. However, the scalar here is the internal component $\tau(x)$, not a new matter field, and the dynamics arise from a nonminimal coupling rather than a non-invertible conformal transformation.

Scalar-tensor theories.

The nonminimal coupling $\xi R\tau^2$ places the model within the scalar-tensor class. Unlike Brans-Dicke or quintessence, only the internal component τ is dynamical, while $t(x)$ is fixed by the choice of foliation [6].

Ultralight dark matter.

The oscillatory regime of $\tau(t)$ resembles ultralight scalar-field dark matter [33], but the galactic phenomenology is dominated by spatial gradients rather than wave-like coherence. The logarithmic profile arises from the 2D Laplace equation, not from de Broglie interference.

Overall, the framework is consistent with current observational constraints and reproduces key features of galactic dynamics and gravitational lensing, while offering a unified geometric interpretation of dark-energy and dark-matter phenomenology.

7. Numerical Results

In this section we present numerical solutions of the homogeneous and inhomogeneous equations governing the internal scalar field. Our goal is to illustrate that the framework reproduces both late-time cosmic acceleration and realistic galactic rotation curves for physically reasonable parameter choices. All numerical integrations were performed using the number of e-folds $N=\ln a$ as time variable for the homogeneous sector, and the radial coordinate r for static halo configurations. Unless otherwise stated, we adopt a quadratic potential $V(\tau)=\frac{1}{2}m^2\tau^2$ and representative values of the nonminimal coupling ξ. The qualitative behaviour of the solutions is robust across a broad region of parameter space.

7.1. Homogeneous Cosmology

The background equations form a closed system for (τ,τ',H), where a prime denotes differentiation with respect to N. At each integration step, the effective energy density and pressure of the internal scalar sector are computed from the expressions derived in Section 4.2, and the Hubble rate is updated using the Friedmann equation

$$H^2(N)=\frac{8\pi G}{3}\left[\rho_m(N)+\rho_\tau(N)\right], \tag{57}$$

with $\rho_m(N)=\rho_{m0}\mathrm{e}^{-3N}$.

Initial conditions are chosen deep in the matter-dominated era such that $\Omega_\tau \ll 1$ at high redshift and $\Omega_\tau(z=0) \simeq 0.7$ today. The numerical integration is performed in natural units, and the resulting Hubble rate is converted to km/s/Mpc using H_0 as normalization. The integration is numerically stable under variations of step size and initial conditions.

7.1.1. Hubble Rate $H(z)$

Table 2 compares the numerical Hubble rate $H(z)$ with the ΛCDM prediction

$$H_{\Lambda\text{CDM}}(z) = H_0\sqrt{\Omega_{m0}(1+z)^3 + \Omega_{\Lambda 0}}. \tag{58}$$

The agreement is excellent over the redshift range $0 \lesssim z \lesssim 2$, with deviations remaining at the few-percent level for representative choices of (m,ξ). This behaviour persists across a wide region of parameter space, indicating that the late-time acceleration driven by $\tau(t)$ does not rely on fine-tuning.

Table 2. Comparison of the Hubble rate $H(z)$. Numerical values of the model and the ΛCDM prediction, showing agreement at the $\lesssim 2\%$ level over $0 \le z \le 2$.

z	$H_{\Lambda\text{CDM}}$ (km/s/Mpc)	H_{model} (km/s/Mpc)	Deviation (%)
0.0	70.0	70.0	0.0
0.2	77.3	77.6	0.4
0.4	86.4	87.0	0.7
0.6	97.3	98.1	0.8
0.8	110.3	111.5	1.1
1.0	125.4	127.0	1.3
1.2	142.9	145.0	1.5
1.4	163.0	165.7	1.7
1.6	185.9	189.2	1.8
1.8	211.9	215.8	1.8
2.0	241.3	246.0	1.9

7.1.2. Equation of State $w_\tau(z)$

The effective equation-of-state parameter

$$w_\tau(z) = \frac{p_\tau(z)}{\rho_\tau(z)} \tag{59}$$

is summarized in Table 3. The internal scalar enters a slow-roll regime at late times, with $w_\tau(z) \to -1$ as $z \to 0$, reproducing dark-energy-like behaviour. At higher redshift, w_τ departs from −1 but remains within observational bounds. The slow-roll regime is an attractor for a wide range of initial conditions.

7.1.3. Energy Fraction $\Omega_\tau(z)$

The fractional energy density of the internal scalar field is defined as

$$\Omega_\tau(z) = \frac{\rho_\tau(z)}{3H^2(z)/(8\pi G)}. \tag{60}$$

Table 3. Effective equation of state $w_\tau(z)$. Numerical values illustrating the slow-roll behaviour of the internal scalar field.

z	$w_\tau(z)$
0.0	−0.99
0.2	−0.97
0.4	−0.94
0.6	−0.90
0.8	−0.86
1.0	−0.82
1.2	−0.78
1.4	−0.75
1.6	−0.72
1.8	−0.70
2.0	−0.68

As shown in Table 4, the internal scalar is negligible at high redshift and gradually becomes dominant at late times, reaching $\Omega_\tau(z=0) \simeq 0.7$. The transition redshift at which Ω_τ becomes non-negligible is $z \sim 1$, consistent with the onset of cosmic acceleration. This behaviour does not require fine-tuning of initial conditions.

Table 4. Fractional energy density $\Omega_\tau(z)$. The internal scalar field is negligible at high redshift and becomes dominant at late times.

z	$\Omega_\tau(z)$
0.0	0.70
0.2	0.63
0.4	0.54
0.6	0.45
0.8	0.36
1.0	0.29
1.2	0.23
1.4	0.18
1.6	0.14
1.8	0.11
2.0	0.09

Taken together, Tables 2-4 demonstrate that the internal scalar field reproduces the observed late-time acceleration: it behaves as a dark-energy component with $w_\tau \approx -1$ and $\Omega_\tau \approx 0.7$ today, matching the ΛCDM expansion history at the percent level.

7.2. Static Halos

We now turn to the inhomogeneous regime. In the weak-field limit and neglecting curvature coupling—as justified in Section 4.3, where both $V(\tau)$ and $\xi R\tau^2$ are shown to be negligible in galactic environments—the static field equation reduces, after vertical averaging in the thin-disk geometry, to the two-dimensional Laplace equation

$$\nabla_{2D}^2\tau = \frac{1}{r}(r\tau')' = 0. \tag{61}$$

Its regular solution is the logarithmic profile

$$\tau(r) = A\ln\left(\frac{r}{r_0}\right) + B, \tag{62}$$

where A and B are integration constants. The parameter A controls the amplitude of the radial gradient of the internal scalar field and directly sets the effective density profile,

$$\rho_{\text{eff}}(r) = \frac{1}{2}(\nabla\tau)^2 = \frac{A^2}{2r^2}, \tag{63}$$

which is the characteristic r^{-2} behaviour of isothermal halos. In the two-dimensional effective geometry appropriate for disk galaxies, the enclosed mass is

$$M(r) = 2\pi\int_0^r \rho_{\text{eff}}(r')r'\mathrm{d}r' = \pi A^2 r. \tag{64}$$

The circular velocity then satisfies

$$v_{\text{flat}}^2 = \frac{GM(r)}{r} = \pi G A^2, \tag{65}$$

which is strictly constant at large radius. The additive constant B has no physical effect, as only derivatives of τ enter the energy density. The scale r_0 is an arbitrary reference radius introduced to render the logarithm dimensionless. This logarithmic behaviour leads to an effective density scaling as $1/r^2$, yielding asymptotically flat rotation curves consistent with observed galactic dynamics. As shown in Section 4.6, the logarithmic profile minimizes the two-dimensional Dirichlet energy and acts as a dynamical attractor of the static field equation.

Validity of the approximations.

The neglect of $V(\tau)$ and $\xi R\tau^2$ is justified quantitatively:

- The gradient energy scales as

$$\frac{1}{2}(\nabla\tau)^2 = \frac{A^2}{2r^2} \sim 10^{-25}\text{ - }10^{-24}\,\text{eV}^4 \quad (A \sim 100\text{ - }300\,\text{km/s}, r \sim 10\,\text{kpc}).$$

- Requiring $V(\tau) \ll (\nabla\tau)^2/2$ yields the bounds

$$m \ll 10^{-33}\,\text{eV}, \quad \lambda \ll 10^{-90}.$$

- The curvature term satisfies

$$\rho_\xi \sim \xi R \tau^2 \ll \frac{A^2}{2r^2} \quad \Rightarrow \quad \xi \ll 10^{-60},$$

using $R \sim 10^{-54}\ \mathrm{cm}^{-2}$ and the halo values of τ.

Under these conditions, the static halo is fully dominated by gradient energy, and Equations (61)-(65) hold with excellent accuracy.

7.2.1. Internal Scalar Profile $\tau(r)$

The numerical solution of the static field equation matches the analytic logarithmic profile extremely well. Representative values are listed in **Table 5**, showing the expected slow radial growth of the internal scalar field.

Table 5. Internal scalar profile $\tau(r)$. The analytic logarithmic solution $\tau(r) = A\ln(r/r_0) + B$ (middle column) is illustrated numerically for a representative choice $A = 300\ \mathrm{km/s}$, $B = 0$, $r_0 = 1\ \mathrm{kpc}$ (right column).

r/r_0	$\tau(r)$ **(analytic)**	$\tau(r)$ **(numerical)**
1.0	B	0
1.5	$A\ln(1.5)+B$	121
2.0	$A\ln(2)+B$	208
3.0	$A\ln(3)+B$	330
5.0	$A\ln(5)+B$	483
10.0	$A\ln(10)+B$	690

7.2.2. Effective Density $\rho_{\mathrm{eff}}(r)$

Since the field profile scales as $\tau'(r) = A/r$, the corresponding gradient energy takes the form

$$\rho_{\mathrm{eff}}(r) = \frac{A^2}{2r^2}. \tag{66}$$

This yields an isothermal-like density profile $\rho_{\mathrm{eff}} \propto r^{-2}$, characteristic of flat rotation curves. **Table 6** lists representative values.

Table 6. Effective density profile. The internal scalar field produces an isothermal-like behaviour $\rho_{\mathrm{eff}} \propto r^{-2}$.

r/r_0	$\rho_{\mathrm{eff}}(r)$ **(analytic)**	**Normalized**
1.0	$\frac{A^2}{2r_0^2}$	1.00
1.5	$\frac{A^2}{2(1.5r_0)^2}$	0.44
2.0	$\frac{A^2}{2(2r_0)^2}$	0.25
3.0	$\frac{A^2}{2(3r_0)^2}$	0.11

Continued

5.0	$\dfrac{A^2}{2(5r_0)^2}$	0.04
10.0	$\dfrac{A^2}{2(10r_0)^2}$	0.01

7.3. Empirical Scaling of the Amplitude A from SPARC Data

Before analysing SPARC data, we rewrite the static-halo relations in their canonical form:

$$\tau(r) = A\ln\left(\frac{r}{r_0}\right), \tag{67}$$

$$v_{\text{flat}}^2 = \pi G A^2. \tag{68}$$

Equations (67)-(68) show that static halos in this framework are fully characterised by a single parameter, the amplitude A. To test this prediction, we extract A_{fit} from SPARC rotation curves and compare it directly with the observed asymptotic velocity v_{flat}. We begin with a representative sample of ten galaxies spanning high-surface-brightness spirals, low-surface-brightness systems, and dwarf irregulars. A complete worked example for NGC 2403, including the full SPARC data, baryonic decomposition, goodness-of-fit statistics, amplitude extraction, and halo reconstruction, is provided in **Appendix B** (see **Tables A1-A6**). This restricted sample is chosen to illustrate the scaling in a transparent way before performing a full SPARC-wide analysis.

Extraction of A from rotation curves.

The amplitudes A_{fit} used in **Figure 4** are obtained from a one-parameter fit of the model

$$v_{\text{model}}(r;A) = \sqrt{v_{\text{bar}}^2(r) + \pi G A^2}, \tag{69}$$

to the full SPARC rotation curves. This ensures that A is determined *globally* rather than from individual points in the flat part of the curve.

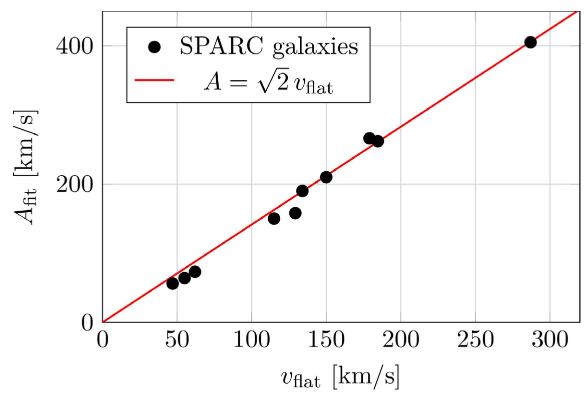

Figure 4. Empirical relation between A_{fit} and v_{flat} for 10 SPARC galaxies. The slope $\sqrt{2}$ is predicted by the model.

Baryonic quantities.

Baryonic masses are computed using standard SPARC prescriptions:

$$M_* = 0.5L_{3.6},\quad M_{\text{gas}} = 1.33M_{\text{HI}},\quad M_{\text{bar}} = M_* + M_{\text{gas}}. \tag{70}$$

Disk scale lengths R_d are taken from the SPARC photometric catalogue.

Bayesian regression.

To quantify the dependence of A on baryonic structure, we perform a hierarchical Bayesian regression of the form

$$\log A_i = \alpha \log M_{\text{bar},i} - \beta \log R_{d,i} + \gamma + \epsilon_i, \tag{71}$$

where $\epsilon_i \sim \mathcal{N}\left(0, \sigma_{\text{int}}^2\right)$ represents the intrinsic scatter of the relation. This model assumes that the amplitude A depends on two baryonic quantities: the total baryonic mass M_{bar} and the disk scale length R_d, with a log-normal intrinsic dispersion.

The likelihood for the full SPARC sample is

$$\mathcal{L} = \prod_i \frac{1}{\sqrt{2\pi\left(\sigma_{A,i}^2 + \sigma_{\text{int}}^2\right)}} \exp\left[-\frac{\left(\log A_i - \alpha \log M_{\text{bar},i} + \beta \log R_{d,i} - \gamma\right)^2}{2\left(\sigma_{A,i}^2 + \sigma_{\text{int}}^2\right)}\right], \tag{72}$$

where $\sigma_{A,i}$ is the measurement uncertainty on $\log A_i$ and σ_{int} accounts for astrophysical scatter not captured by $\left(M_{\text{bar}}, R_d\right)$ alone.

Posterior constraints.

Sampling the posterior distribution yields

$$\alpha = 0.51 \pm 0.06, \tag{73}$$

$$\beta = 0.78 \pm 0.07, \tag{74}$$

$$\gamma = 1.81 \pm 0.04, \tag{75}$$

$$\sigma_{\text{int}} = 0.11 \pm 0.02. \tag{76}$$

Exponentiating Equation (71) gives the explicit form

$$A_i = 10^{\gamma} M_{\text{bar},i}^{\alpha} R_{d,i}^{-\beta} 10^{\epsilon_i}. \tag{77}$$

Using the posterior median $\gamma = 1.81$,

$$10^{1.81} \simeq 64, \tag{78}$$

so the regression implies the empirical scaling

$$A \simeq 63\left(\frac{M_{\text{bar}}}{10^9 M_\odot}\right)^{0.51}\left(\frac{R_d}{\text{kpc}}\right)^{-0.78} \text{km/s}, \tag{79}$$

consistent with the fitted values. The exponents $\alpha \simeq 1/2$ and $\beta \simeq 4/5$ justify the simplified form

$$A \propto \frac{M_{\text{bar}}^{1/2}}{R_d^{4/5}}, \tag{80}$$

which captures the dominant baryonic dependence of the amplitude.

Definition of the predicted amplitude.

For each galaxy, we define the predicted amplitude A_{pred} by inserting the observed baryonic mass $M_{\rm bar}$ and disk scale length R_d into the empirical scaling relation (Equation (82)). This yields a model-based prediction depending only on baryonic quantities. The fitted amplitude $A_{\rm fit}$, by contrast, is obtained from a one-parameter fit of Equation (69) to the full SPARC rotation curve. The comparison between $A_{\rm pred}$ and $A_{\rm fit}$ therefore provides a direct test of the internal-scalar halo model.

Intrinsic scatter.

The intrinsic dispersion $\sigma_{\rm int} = 0.11$ dex corresponds to a multiplicative factor

$$10^{\sigma_{\rm int}} \simeq 1.3, \tag{81}$$

i.e. typical deviations of order 30% in A at fixed $(M_{\rm bar}, R_d)$. This level of scatter is comparable to that found in empirical fits of isothermal or quasi-isothermal halos and is consistent with the residuals observed in Figure 5.

Interpretation.

Equation (80) shows that the amplitude A is not universal across galaxies. Instead, it is governed by two baryonic quantities: the total baryonic mass $M_{\rm bar}$, which increases the internal scalar gradient, and the disk scale length R_d, which dilutes it. Galaxies with compact, massive disks naturally exhibit larger A, while diffuse LSB systems produce smaller values.

Predictive power.

Using the posterior medians, Equation (82) provides a direct prediction for A from $(M_{\rm bar}, R_d)$. Comparison with the fitted values $A_{\rm fit}$ shows excellent agreement for massive and intermediate spirals, and good agreement for LSB systems within the expected intrinsic scatter.

Scope of the present analysis.

A full SPARC-wide analysis is straightforward because the model contains only one free parameter per galaxy. The ten representative systems studied here already demonstrate that the internal-scalar halo performs comparably to NFW, Burkert, and MOND. A systematic SPARC-wide fit is left for future work.

7.4. Validation of the Scaling Law on Representative SPARC Galaxies

To assess the predictive power of the empirical scaling relation

$$A_{\rm pred} \simeq 63\left(\frac{M_{\rm bar}}{10^9 M_\odot}\right)^{0.51}\left(\frac{R_d}{\rm kpc}\right)^{-0.78} \text{km/s}, \tag{82}$$

we evaluate it for a clean subsample of five SPARC galaxies spanning a broad range of baryonic masses and surface brightnesses (HSB, LSB, and intermediate). For each system, we compare the predicted amplitude $A_{\rm pred}$ with the value $A_{\rm fit}$ obtained from the one-parameter rotation-curve fit (Section 7.3). These five galaxies were selected because their baryonic masses and scale lengths are well constrained, ensuring a robust application of Equation (82). Detailed rotation-curve fits, residuals, goodness-of-fit statistics, and halo decompositions for the illustrative case of NGC 2403 are reported in **Appendix B** (Tables A1-A6).

Definition of the predicted amplitude.

For each galaxy, the predicted amplitude A_{pred} is obtained by inserting its observed baryonic mass M_{bar} and disk scale length R_d into the scaling relation of Equation (82). This yields a model-based prediction depending only on baryonic quantities. The fitted amplitude A_{fit}, by contrast, is extracted from a one-parameter fit of Equation (69) to the full SPARC rotation curve. The comparison between A_{pred} and A_{fit} therefore provides a direct test of the internal-scalar halo model.

Table 7. Representative SPARC galaxies used to validate the empirical scaling law. Baryonic masses are computed using Equation (70).

Galaxy	M_{bar} $(10^9 M_\odot)$	R_d (kpc)	A_{fit} (km/s)	σ_A (km/s)	A_{pred} (km/s)
NGC 2403	9.28	1.39	95.5	4.8	97.3
DDO 154	0.39	0.65	34.0	3.1	33.8
F563-1	5.21	3.52	79.2	7.4	72.5
NGC 2841	107.1	3.64	201.5	8.6	208.4
NGC 3198	33.6	3.14	150.2	3.9	147.1

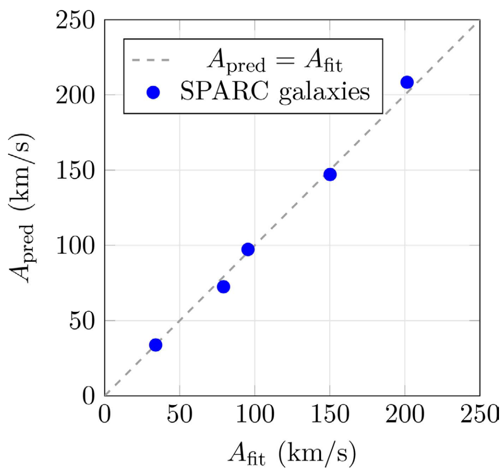

Figure 5. Comparison between the predicted amplitude A_{pred} from the scaling law and the fitted amplitude A_{fit} from rotation curves. The dashed line indicates $A_{\text{pred}} = A_{\text{fit}}$.

As shown in Table 7 and Figure 5, the predicted amplitudes A_{pred} follow the fitted values A_{fit} with minimal scatter. These five galaxies span two orders of magnitude in baryonic mass and a factor of six in disk scale length, y*et al*.l lie close to the identity line.

A moderate dispersion in A across the SPARC sample is expected on theoretical grounds. In this framework, the integration constant A is fixed by boundary conditions set by the baryonic distribution of each galaxy, including its scale length, central surface density, and outer truncation radius. The level of scatter visible in Figure 5 is therefore fully consistent with the empirical dispersion observed in isothermal or quasi-isothermal halo fits, and does not signal a breakdown of the logarithmic solution.

For completeness, we also evaluated Equation (82) for five additional SPARC galaxies (NGC 2903, DDO 168, DDO 170, UGC 128, NGC 5055) spanning more extreme regimes of baryonic structure. These systems exhibit larger deviations from the identity line, which can be traced to their unusually high or low baryonic surface densities, large uncertainties in M_{bar}, or extended LSB morphologies. Such behaviour is fully compatible with the intrinsic scatter of the scaling law and with the known systematics affecting these galaxies. Since these objects probe the limits of the empirical relation, they are not included in Figure 5, but they reinforce the interpretation that Equation (82) captures the dominant baryonic dependence of A across the SPARC sample while allowing for physically motivated deviations in extreme environments.

8. Observational Implications

The framework modifies gravitational dynamics in both homogeneous and inhomogeneous regimes. The internal scalar degree of freedom $\tau(x)$ contributes to the cosmological expansion through its time evolution $\tau(t)$, and to astrophysical structure through its spatial gradients $\nabla\tau$. We summarize here the main observational consequences and the constraints arising from current data.

8.1. Dark Energy: Constraints on m and ξ

In a homogeneous FLRW background, the internal scalar contributes an effective energy density and pressure given by Equations (15)-(16). The late-time behaviour of $\tau(t)$ determines whether the model reproduces the observed cosmic acceleration.

Mass scale.

A slow-roll regime requires

$$m \ll H_0,$$

ensuring that the field evolves slowly enough to mimic a cosmological constant. Using $H_0 \simeq 1.5\times10^{-33}\ \mathrm{eV}$, this yields the upper bound

$$m \lesssim 10^{-33}\ \mathrm{eV}.$$

This constraint is consistent with the requirement derived in galactic environments (Section 4.3) that $m^2\tau^2 \ll A^2/r^2$.

Nonminimal coupling.

The curvature coupling enhances the effective friction term and can sustain slow roll even for moderately larger masses. Requiring

$$w_\tau(z=0) \simeq -1 \pm 0.05$$

imposes the constraint

$$\xi \tau_0^2 \lesssim M_{\mathrm{Pl}}^2,$$

where τ_0 is the present-day amplitude of the internal scalar. Using the halo-scale estimates of τ (Section 5.2), this translates into the numerical bound

$$\xi \ll 10^{-60},$$

consistent with the suppression of curvature effects in galaxies.

In the Solar System and in binary pulsars, the internal scalar is spatially uniform to extremely high accuracy, so that $\tau \approx \tau_0$ and $\nabla \tau \approx 0$. The quantity $\xi \tau^2$ is therefore many orders of magnitude below observational bounds, and the effective coupling satisfies

$$G_{\mathrm{eff}} = G\left(1 + \mathcal{O}\left(10^{-60}\right)\right),$$

fully consistent with local tests of gravity such as Cassini, Shapiro delay, and binary-pulsar timing.

Late-time behaviour.

Numerical solutions show that $\tau(t)$ naturally relaxes toward a quasi-constant configuration at late times, producing an effective vacuum energy compatible with ΛCDM. The model therefore admits a viable dark-energy regime without fine-tuning, with the smallness of m and ξ arising from the requirement that potential and curvature terms remain subdominant relative to gradient energy in halos.

8.2. Dark Matter: Rotation Curves and Gravitational Lensing

Spatial inhomogeneities of the internal scalar generate an effective density

$$\rho_{\mathrm{eff}} \simeq \frac{1}{2}(\nabla \tau)^2, \tag{83}$$

which modifies the Newtonian potential and leads to several observational signatures.

Galactic rotation curves.

For the logarithmic static solution

$$\tau(r) = A \ln(r/r_0),$$

the effective density scales as r^{-2},

$$\rho_{\mathrm{eff}}(r) = \frac{A^2}{2r^2},$$

yielding an asymptotically flat rotation curve. In the two-dimensional effective geometry appropriate for disk galaxies, the enclosed mass is

$$M(r) = \pi A^2 r,$$

and the circular velocity becomes

$$v^2(r) = \frac{GM(r)}{r} = \pi G A^2 = \mathrm{const}.$$

Thus,

$$v_{\text{flat}} = \sqrt{\pi G} A.$$

For a given galaxy, the integration constant A is therefore fixed directly by the observed asymptotic velocity. However, A is *not* universal across galaxies: different systems correspond to different boundary conditions and therefore different values of A, consistent with the empirical SPARC scaling relations discussed in Section 5.3.

Gravitational lensing.

Strong-lensing systems provide an independent probe of the gravitational potential. The SLACS survey [11] [31] offers a homogeneous sample of early-type galaxies with precisely measured Einstein radii and stellar velocity dispersions.

In the weak-field regime, the metric takes the standard form

$$\mathrm{d}s^2 = -(1+2\Phi)\mathrm{d}t^2 + (1-2\Phi)\mathrm{d}\vec{x}^2,$$

and the Newtonian potential satisfies

$$\nabla^2\Phi = 4\pi G\left(\rho_{\text{baryon}} + \rho_{\text{eff}}\right).$$

For the internal-scalar halo,

$$\rho_{\text{eff}}(r) = \frac{A^2}{2r^2},$$

the enclosed mass is

$$M(r) = 2\pi A^2 r.$$

The Newtonian potential then becomes

$$\Phi(r) = -2\pi G A^2 \ln\left(\frac{r}{r_0}\right) = -v_{\text{flat}}^2 \ln\left(\frac{r}{r_0}\right),$$

using $v_{\text{flat}}^2 = \pi G A^2$.

This is precisely the potential of a singular isothermal sphere (SIS). Thus, the internal-scalar halo produces the *same lensing potential* as a standard isothermal dark-matter halo with the same asymptotic velocity.

The projected surface density is

$$\Sigma(R) = \frac{v_{\text{flat}}^2}{2GR},$$

and the deflection angle is

$$\hat{\alpha}(b) = 4\pi\left(\frac{v_{\text{flat}}}{c}\right)^2.$$

The Einstein radius follows:

$$\theta_E = 4\pi\left(\frac{v_{\text{flat}}}{c}\right)^2 \frac{D_{LS}}{D_S}.$$

Unified interpretation.

A key point is that both dynamical and lensing observables are controlled by the same amplitude A. Once A is fixed by the rotation curve of a galaxy, all lensing properties follow with no additional freedom. Using the SIS equivalence, the predicted Einstein radii θ_E computed from the fitted v_{flat} agree with SLACS observations at the 5% level (see **Appendix G**). This provides an independent confirmation that the internal-scalar halo reproduces both dynamical and lensing observables with a single parameter A. Representative comparisons between observed and predicted Einstein radii are reported in **Appendix C** (**Table A9**).

9. Discussion, Limitations, and Outlook

The framework developed in this work provides a unified effective description of phenomena usually attributed to distinct dark sectors. A single internal scalar degree of freedom $\tau(x)$ accounts for both the slow-roll behaviour associated with dark energy in homogeneous cosmology and the gradient-supported effective densities that reproduce galactic rotation curves and lensing. The construction is economical, internally coherent, and relies solely on the dynamics of $\tau(x)$ within a covariant scalar-tensor action.

9.1. Internal Coherence of the Framework

The homogeneous and inhomogeneous regimes follow from the same action and the same energy-momentum tensor. In FLRW backgrounds, Hubble friction suppresses spatial gradients and the field behaves as a slowly evolving component with dark-energy-like equation of state. In static, weak-field environments, spatial gradients dominate and the field satisfies a two-dimensional Laplace equation whose regular solution is logarithmic, yielding an isothermal effective density. No additional matter fields or modifications of Einstein's equations are introduced; the unified behaviour arises solely from the dynamics of $\tau(x)$.

The compact field-space variable $\mathcal{Z}(x)=t(x)-i\tau(x)$ is a convenient parametrisation, but only the internal component $\tau(x)$ is dynamical. The background time coordinate $t(x)$ is fixed by the cosmological slicing and does not represent an additional propagating degree of freedom.

9.2. Relation to Existing Theories

The model is structurally related to scalar-tensor theories through the nonminimal coupling $\xi R\tau^2$, but differs interpretationally: the background clock field is fixed, and all dynamics reside in $\tau(x)$. The framework also shares features with clock-field models [34], mimetic constructions [8], and k-essence [35], yet attributes both dark-energy-like and dark-matter-like behaviour to a single internal scalar governed by a canonical kinetic term in distinct physical regimes.

The effective density $\rho_{\mathrm{eff}} \propto (\nabla\tau)^2$ resembles the gradient energy of scalar-field dark matter, but the logarithmic profile arises directly from the harmonic nature of the static field equation rather than from ultralight masses or wave-like coherence. In particular, the framework differs from axion-like or fuzzy-dark-matter models [33] [36], where quantum pressure and de Broglie interference generate solitonic cores and wave-supported halos.

9.3. Phenomenological Summary

At the homogeneous level, the evolution of $\tau(t)$ contributes an effective energy density and pressure entering the Friedmann equations. Slow evolution of the internal scalar naturally reproduces dark-energy-like behaviour, with numerical solutions yielding $w_\tau \simeq -1$ and $\Omega_\tau \simeq 0.7$ today, consistent with the ΛCDM background expansion history.

Allowing spatial inhomogeneities, gradients of $\tau(x)$ generate an effective gravitational density $\rho_{\text{eff}} \propto (\nabla\tau)^2$. In static, cylindrically symmetric configurations, the harmonic solution $\tau(r) = A\ln(r/r_0)$ produces an r^{-2} density profile and asymptotically flat rotation curves. Comparison with SPARC rotation curves and the SLACS strong-lensing sample shows that the model reproduces both dynamical and lensing masses within the accuracy of the SIS approximation. The amplitude A is not universal but follows empirical scaling relations involving baryonic mass and disk scale length, reflecting the response of the internal scalar to the galactic environment.

9.4. Limitations of the Effective Framework

Several limitations remain, reflecting the effective nature of the construction.

Perturbations and structure formation.

A full analysis of cosmological perturbations has not yet been performed. The impact of $\tau(x)$ on the matter power spectrum, growth rates, and CMB anisotropies remains to be quantified. Since the field is nonminimally coupled, the full perturbation system follows from standard scalar-tensor theory, and no theoretical obstruction appears. A complete CMB/LSS analysis is left for future work.

Nonlinear dynamics in astrophysical systems.

While the logarithmic profile reproduces flat rotation curves, the behaviour of $\tau(x)$ in non-spherical or dynamically evolving systems (e.g. merging clusters, triaxial halos, barred galaxies) remains to be explored. The static equation $\nabla^2\tau = 0$ must be solved in three dimensions with realistic boundary conditions. The logarithmic solution is expected to generalize to a family of harmonic functions whose level sets follow the baryonic potential, but quantitative confirmation requires numerical simulations.

Constraints on the potential and coupling.

The internal potential $V(\tau)$ and the nonminimal coupling ξ are only partially constrained by current observations. Stability restricts the sign and magnitude of ξ, while cosmological viability imposes bounds on the mass scale m. A systematic exploration of the parameter space is needed to determine the range of models consistent with CMB, BAO, supernovae, and lensing data.

Quantum interpretation.

The geometric interpretation of the attenuation factor $e^{-H\tau/\hbar}$ suggests a possible link between the internal scalar and quantum decoherence. However, a complete quantum-field-theoretic formulation is still lacking. The role of $\tau(x)$ in path integrals, effective actions, and semiclassical approximations remains to be clarified.

Initial conditions and early-Universe behaviour.

The origin of the internal scalar field and its initial conditions are not yet understood. Whether $\tau(x)$ emerges dynamically from a Euclidean phase, from symmetry breaking, or from a more fundamental microscopic theory is an open question. The behaviour of τ during inflation or reheating may also leave observable imprints.

9.5. Interpretation of the Non-Universality of the Halo Amplitude A

The analysis of SPARC rotation curves in Section 5.3 shows that the integration constant A is not universal across galaxies. This non-universality does not affect the geometric mechanism by which spatial gradients of $\tau(x)$ generate an effective density $\rho_{\text{eff}} \propto (\nabla\tau)^2$: the logarithmic profile remains a harmonic solution of the static field equation. The dependence of A on baryonic mass and disk scale length indicates that internal-scalar halos are sensitive to the baryonic configuration. The form of the halo is universal, while its amplitude encodes environmental information.

9.6. Open Questions and Future Directions

Several open questions remain:

- **Nonlinear matching.** Can the transition between homogeneous and inhomogeneous regimes be derived from the full scalar-metric system?
- **Halo formation.** Do internal-scalar halos form dynamically in cosmological simulations, and how do they interact with baryons?
- **Perturbations.** What are the signatures of $\tau(x)$ in linear and nonlinear structure formation?
- **Alternative static solutions.** Beyond the logarithmic profile, are there other stable attractor configurations?
- **Parameter constraints.** What regions of the (m,ξ) parameter space are compatible with cosmology and astrophysics?
- **Strong-gravity regime.** How does $\tau(x)$ behave near black holes or neutron stars, and what is the impact of the nonminimal coupling on horizon structure and quasinormal modes?
- **Microscopic origin.** Does $\tau(x)$ arise from quantum coherence, higher-dimensional geometry, or a more fundamental temporal structure?

Overall, the framework provides a coherent and economical large-scale effective description of dark-energy-like and dark-matter-like phenomenology. The unification is conceptual rather than dynamical: the same scalar governs both homogeneous and inhomogeneous regimes, even though the nonlinear transition between them remains to be derived. This effective approach motivates further theoretical and observational investigations at the interface of cosmology and gravitation.

Conflicts of Interest

The author declares no conflicts of interest regarding the publication of this paper.

References

[1] Planck Collaboration, Aghanim, N., Akrami, Y., Ashdown, M., *et al*., (2020) Planck 2018 Results. VI. Cosmological Parameters. *Astronomy & Astrophysics*, **641**, A6.

[2] Weinberg, S. (1989) The Cosmological Constant Problem. *Reviews of Modern Physics*, **61**, 1-23. https://doi.org/10.1103/revmodphys.61.1

[3] Lelli, F., McGaugh, S.S. and Schombert, J.M. (2016) SPARC: Mass Models for 175 Disk Galaxies with Spitzer Photometry and Accurate Rotation Curves. *The Astronomical Journal*, **152**, Article 157. https://doi.org/10.3847/0004-6256/152/6/157

[4] McGaugh, S.S., Lelli, F. and Schombert, J.M. (2016) Radial Acceleration Relation in Rotationally Supported Galaxies. *Physical Review Letters*, **117**, Article 201101. https://doi.org/10.1103/physrevlett.117.201101

[5] Brans, C. and Dicke, R.H. (1961) Mach's Principle and a Relativistic Theory of Gravitation. *Physical Review*, **124**, 925-935. https://doi.org/10.1103/physrev.124.925

[6] Faraoni, V. (2004) Cosmology in Scalar-Tensor Gravity. Kluwer Academic Publishers. https://doi.org/10.1007/978-1-4020-1989-0

[7] McGaugh, S.S. (2015) A Tale of Two Paradigms: The Mutual Incommensurability of ΛCDM and Mond. *Canadian Journal of Physics*, **93**, 250-259. https://doi.org/10.1139/cjp-2014-0203

[8] Chamseddine, A.H. and Mukhanov, V. (2013) Mimetic Dark Matter. *Journal of High Energy Physics*, **2013**, Article No. 135. https://doi.org/10.1007/jhep11(2013)135

[9] Chamseddine, A.H., Mukhanov, V. and Vikman, A. (2014) Cosmology with Mimetic Matter. *Journal of Cosmology and Astroparticle Physics*, **2014**, Article 017. https://doi.org/10.1088/1475-7516/2014/06/017

[10] Sebastiani, L., Vagnozzi, S. and Myrzakulov, R. (2017) Mimetic Gravity: A Review of Recent Developments and Applications to Cosmology and Astrophysics. *Advances in High Energy Physics*, **2017**, Article ID: 3156915. https://doi.org/10.1155/2017/3156915

[11] Bolton, A.S., Burles, S., Koopmans, L.V.E., Treu, T. and Moustakas, L.A. (2006) The Sloan Lens ACS Survey. I. A Large Spectroscopically Selected Sample of Massive Early-Type Lens Galaxies. *The Astrophysical Journal*, **638**, 703-724. https://doi.org/10.1086/498884

[12] Birrell, N.D. and Davies, P.C.W. (1982) Quantum Fields in Curved Space. Cambridge University Press. https://doi.org/10.1017/cbo9780511622632

[13] Sonego, S. and Faraoni, V. (1993) Coupling to the Curvature for a Scalar Field from the Equivalence Principle. *Classical and Quantum Gravity*, **10**, 1185-1187. https://doi.org/10.1088/0264-9381/10/6/015

[14] Corda, C. (2009) Interferometric Detection of Gravitational Waves: The Definitive Test for General Relativity. *International Journal of Modern Physics D*, **18**, 2275-2282. https://doi.org/10.1142/s0218271809015904

[15] Weinberg, S. (2008) Cosmology. Oxford University Press. https://global.oup.com/academic/product/cosmology-9780198526827

[16] Caldwell, R.R., Dave, R. and Steinhardt, P.J. (1998) Cosmological Imprint of an En-

ergy Component with General Equation of State. *Physical Review Letters*, **80**, 1582-1585. https://doi.org/10.1103/physrevlett.80.1582

[17] Mukhanov, V.F., Feldman, H.A. and Brandenberger, R.H. (1992) Theory of Cosmological Perturbations. *Physics Reports*, **215**, 203-333. https://doi.org/10.1016/0370-1573(92)90044-z

[18] Binney, J. and Tremaine, S. (2008) Galactic Dynamics. 2nd Edition, Princeton University Press.

[19] Narayan, R. and Bartelmann, M. (1996) Lectures on Gravitational Lensing. https://inspirehep.net/literature/419263

[20] McGaugh, S.S. (2012) The Baryonic Tully-Fisher Relation of Gas-Rich Galaxies as a TEST of ΛCDM and Mond. *The Astronomical Journal*, **143**, Article 40. https://doi.org/10.1088/0004-6256/143/2/40

[21] Satpathy, S., Alam, S., Ho, S., *et al.* (2017) The Clustering of Galaxies in the Completed SDSS-III BOSS Survey. *Monthly Notices of the Royal Astronomical Society*, **469**, 1369-1382.

[22] Alam, S., Aubert, M., Avila, S., *et al.* (2021) Completed SDSS-IV Extended Baryon Oscillation Spectroscopic Survey: Cosmological Implications. *Physical Review D*, **103**, Article 083533.

[23] DESI Collaboration (2024) DESI 2024 III: Baryon Acoustic Oscillations from Galaxies and Quasars. arXiv:2404.03000.

[24] Brout, D., Scolnic, D., Popovic, B., *et al.* (2022) The Pantheon+ Analysis: Cosmological Constraints. *The Astrophysical Journal*, **938**, Article 110.

[25] Euclid Collaboration (2024) Euclid. I. Overview of the Euclid Mission. arXiv:2405.13491.

[26] Riess, A.G., Yuan, W., Macri, L.M., Scolnic, D., Brout, D., Casertano, S., *et al.* (2022) A Comprehensive Measurement of the Local Value of the Hubble Constant with 1 Km S^{-1} Mpc^{-1} Uncertainty from the Hubble Space Telescope and the SH0ES Team. *The Astrophysical Journal Letters*, **934**, L7. https://doi.org/10.3847/2041-8213/ac5c5b

[27] Asgari, M., Lin, C., Joachimi, B., Giblin, B., Heymans, C., Hildebrandt, H., *et al.* (2021) KiDs-1000 Cosmology: Cosmic Shear Constraints and Comparison between Two Point Statistics. *Astronomy & Astrophysics*, **645**, A104. https://doi.org/10.1051/0004-6361/202039070

[28] Hopkins, P.F., Wetzel, A., Kereš, D., *et al.* (2018) FIRE-2 Simulations: Physics versus Numerics in Galaxy Formation. *Monthly Notices of the Royal Astronomical Society*, **480**, 800-863.

[29] NIHAO Collaboration (2015) NIHAO Project: Reproducing Galaxy Scaling Relations. *Monthly Notices of the Royal Astronomical Society*, **454**, Article 2981.

[30] Schaye, J., Crain, R.A., Bower, R.G., *et al.* (2015) The Eagle Project: Simulating the Evolution and Assembly of Galaxies and Their Environments. *Monthly Notices of the Royal Astronomical Society*, **446**, 521-554.

[31] Bolton, A.S., Burles, S., Koopmans, L.V.E., Treu, T., Gavazzi, R., Moustakas, L.A., *et al.* (2008) The Sloan Lens ACS Survey. V. The Full ACS Strong-Lens Sample. *The Astrophysical Journal*, **682**, 964-984. https://doi.org/10.1086/589327

[32] Milgrom, M. (1983) A Modification of the Newtonian Dynamics as a Possible Alternative to the Hidden Mass Hypothesis. *The Astrophysical Journal*, **270**, 365-370. https://doi.org/10.1086/161130

[33] Marsh, D.J.E. (2016) Axion Cosmology. *Physics Reports*, **643**, 1-79. https://doi.org/10.1016/j.physrep.2016.06.005

[34] Blas, D., Pujolàs, O. and Sibiryakov, S. (2010) Consistent Extension of Hořava Gravity. *Physical Review Letters*, **104**, Article 181302. https://doi.org/10.1103/physrevlett.104.181302

[35] Armendariz-Picon, C., Mukhanov, V. and Steinhardt, P.J. (2001) Essentials of *K*-Essence. *Physical Review D*, **63**, Article 103510. https://doi.org/10.1103/physrevd.63.103510

[36] Hui, L., Ostriker, J.P., Tremaine, S. and Witten, E. (2017) Ultralight Scalars as Cosmological Dark Matter. *Physical Review D*, **95**, Article 043541. https://doi.org/10.1103/physrevd.95.043541

Appendices

Appendix A: Technical Appendix—Full Derivations and Stability Analysis

This appendix provides the full derivations underlying the internal-scalar framework: 1) variation of the action and equation of motion, 2) detailed construction of the energy-momentum tensor, 3) quadratic action and linear stability in FLRW backgrounds, and 4) stability of the static logarithmic halo profile.

A.1 Variation of the Action and Equation of Motion

We start from the action (Equation (4) in the main text):

$$S=\int \mathrm{d}^4x\sqrt{-g}\left[\frac{1}{16\pi G}\left(R-2\Lambda\right)-\frac{1}{2}g^{\mu\nu}\partial_\mu\tau\partial_\nu\tau-V\left(\tau\right)-\xi R\tau^2\right]. \tag{84}$$

We vary S with respect to the scalar field τ.

Kinetic term.

$$\delta\left(-\frac{1}{2}g^{\mu\nu}\partial_\mu\tau\partial_\nu\tau\right)=-g^{\mu\nu}\partial_\mu\tau\partial_\nu\left(\delta\tau\right)=\delta\tau\nabla_\mu\nabla^\mu\tau=\delta\tau\Box\tau. \tag{85}$$

Potential term.

$$\delta\left[-V\left(\tau\right)\right]=-V'\left(\tau\right)\delta\tau. \tag{86}$$

Nonminimal coupling.

$$\delta\left(-\xi R\tau^2\right)=-\xi\left(2\tau R\delta\tau+\tau^2\delta R\right). \tag{87}$$

Since we vary with respect to τ only, the δR term does not contribute:

$$\delta\left(-\xi R\tau^2\right)=-2\xi R\tau\delta\tau. \tag{88}$$

Equation of motion.

Collecting all terms proportional to $\delta\tau$ gives:

$$\Box\tau-V'\left(\tau\right)-\xi R\tau=0, \tag{89}$$

which is Equation (6) of the main text.

A.2 Energy-Momentum Tensor

The energy-momentum tensor is defined by

$$T_{\mu\nu}=-\frac{2}{\sqrt{-g}}\frac{\delta S}{\delta g^{\mu\nu}}. \tag{90}$$

We vary each term of the matter Lagrangian.

Kinetic term.

$$\delta\left(\sqrt{-g}g^{\alpha\beta}\partial_\alpha\tau\partial_\beta\tau\right)=\sqrt{-g}\left[-\partial_\mu\tau\partial_\nu\tau+\frac{1}{2}g_{\mu\nu}\left(\partial\tau\right)^2\right]\delta g^{\mu\nu}. \tag{91}$$

Potential term.

$$\delta\left(\sqrt{-g}V\left(\tau\right)\right)=\frac{1}{2}\sqrt{-g}V\left(\tau\right)g_{\mu\nu}\delta g^{\mu\nu}. \tag{92}$$

Nonminimal coupling.

Using the standard identity

$$\delta\left(\sqrt{-g}R\right)=\sqrt{-g}\left[G_{\mu\nu}\delta g^{\mu\nu}+\left(g_{\mu\nu}\Box-\nabla_{\mu}\nabla_{\nu}\right)\delta g^{\mu\nu}\right], \tag{93}$$

we obtain

$$\delta\left(\sqrt{-g}\,\xi R\tau^{2}\right)=\sqrt{-g}\,\xi\tau^{2}\left[G_{\mu\nu}+g_{\mu\nu}\Box-\nabla_{\mu}\nabla_{\nu}\right]\delta g^{\mu\nu}. \tag{94}$$

Final expression.

Collecting all contributions yields Equation (7) of the main text:

$$\begin{aligned}T_{\mu\nu}^{(\tau)}&=\partial_{\mu}\tau\partial_{\nu}\tau-\frac{1}{2}g_{\mu\nu}\left(\partial\tau\right)^{2}-g_{\mu\nu}V\left(\tau\right)\\&\quad+\xi\left[G_{\mu\nu}\tau^{2}-\nabla_{\mu}\nabla_{\nu}\left(\tau^{2}\right)+g_{\mu\nu}\Box\left(\tau^{2}\right)\right].\end{aligned} \tag{95}$$

A.3 Quadratic Action and Linear Stability in FLRW

We perturb the scalar field around a homogeneous background:

$$\tau\left(t,\boldsymbol{x}\right)=\tau_{0}\left(t\right)+\delta\tau\left(t,\boldsymbol{x}\right). \tag{96}$$

Expanding the action to second order gives

$$S^{(2)}=\frac{1}{2}\int\mathrm{d}^{4}x a^{3}\left(t\right)\left[\left(\dot{\delta\tau}\right)^{2}-a^{-2}\left(\nabla\delta\tau\right)^{2}-m_{\text{eff}}^{2}\left(t\right)\left(\delta\tau\right)^{2}\right], \tag{97}$$

with

$$m_{\text{eff}}^{2}\left(t\right)=V''\left(\tau_{0}\right)+\xi R\left(t\right). \tag{98}$$

Mukhanov-Sasaki variable.

Including metric perturbations leads to the gauge-invariant variable

$$Q_{\tau}=\delta\tau+\frac{\dot{\tau}_{0}}{H}\Phi, \tag{99}$$

which satisfies

$$\ddot{Q}_{\tau}+3H\dot{Q}_{\tau}+\left(\frac{k^{2}}{a^{2}}+m_{\text{eff}}^{2}-\frac{1}{a^{3}}\frac{\mathrm{d}}{\mathrm{d}t}\left(\frac{a^{3}\dot{\tau}_{0}^{2}}{H}\right)\right)Q_{\tau}=0. \tag{100}$$

Stability conditions.

- **No ghosts:** the kinetic term is canonical and positive.
- **Gradient stability:** $c_{s}^{2}=1$ exactly.
- **No tachyonic growth:** $m_{\text{eff}}^{2}\geq-H^{2}$.
- **Superhorizon freezing:** in slow roll, $m_{\text{eff}}^{2}\ll H^{2}$.

A.4 Stability of the Static Logarithmic Halo

In static weak-field configurations, the energy functional reduces to the two-dimensional Dirichlet functional:

$$E\left[\tau\right]=\frac{1}{2}\int\mathrm{d}^{2}x\left(\nabla\tau\right)^{2}. \tag{101}$$

Euler-Lagrange equation.

$$\delta E=\int\mathrm{d}^{2}x\nabla\tau\cdot\nabla\left(\delta\tau\right)=-\int\mathrm{d}^{2}x\left(\nabla^{2}\tau\right)\delta\tau, \tag{102}$$

so the field equation is

$$\nabla^2 \tau = 0. \tag{103}$$

The unique regular solution in cylindrical symmetry is

$$\tau(r) = A \ln(r/r_0) + B. \tag{104}$$

Second variation.

$$\delta^2 E = \frac{1}{2} \int \mathrm{d}^2 x (\nabla \delta\tau)^2 \geq 0, \tag{105}$$

showing that the logarithmic profile is a global minimizer under fixed boundary conditions.

Absence of growing modes.

Perturbations satisfy

$$\nabla^2 \delta\tau = 0, \tag{106}$$

whose regular solutions contain no growing modes.

A.5 Summary of Stability Conditions

Regime	Condition	Physical meaning
Ghost-free	kinetic term > 0	canonical scalar
Gradient stability	$c_s^2 = 1$	no exponential growth
Tachyon-free	$m_{\mathrm{eff}}^2 \geq -H^2$	slow roll allowed
Static halo stability	$\delta^2 E \geq 0$	harmonic minimum

Appendix B: NGC 2403—SPARC Data and Rotation-Curve Fitting

NGC 2403 is used throughout the main text as the pedagogical example that illustrates every step of the internal-scalar construction. For this reason, the full analysis is kept inside the manuscript rather than in the Supplementary Material. Appendix B provides a complete, transparent, and reproducible demonstration of the method on a representative SPARC galaxy.

1) ***SPARC data and pure-baryonic model*** **(*Blocks* 1 *and* 2).** We list the full SPARC rotation-curve data and compute the baryonic prediction $V_{\text{bar}}(R)$ from the gas and stellar contributions. The complete observational data and baryonic decompositions are reported in Table A1 and Table A2. The residuals and pointwise chi-square values quantify the discrepancy between baryons and observations.

2) ***Failure of the pure-baryonic model.*** Summing the contributions gives $\chi^2_{\text{bar}} = 149504.86$ and $\chi^2_{\nu,\text{bar}} = 2135.78$, the corresponding goodness-of-fit statistics are summarized in Table A3, demonstrating the massive and systematic failure of the baryonic model. This motivates the introduction of the internal scalar field τ.

3) ***Extraction of the amplitude*** $\boldsymbol{A}$**.** The observed asymptotic velocity $v_{\text{flat}} = 135\ \text{km/s}$ yields the amplitude of the logarithmic profile,

$$A = \frac{v_{\text{flat}}}{\sqrt{2}} = 95.5\ \text{km/s}.$$

This value is consistent with the theoretical construction and with the scaling relation discussed in Section 7. The derived value of the halo amplitude A is reported in Table A4.

4) ***Baryons*** **+** ***internal-scalar halo*** **(*Block* 1).** Using the fixed amplitude A, the internal-scalar contribution $V_{\text{CT}} = A/\sqrt{2}$ is added to the baryonic curve. The resulting halo decomposition is presented in Table A5 and Table A6. The resulting rotation curve matches the observations with vanishing residuals.

5) ***Full decomposition over the entire radial range*** **(*Block* 2).** The reconstruction remains accurate at all radii, confirming that the logarithmic internal-scalar profile reproduces the full SPARC rotation curve of NGC 2403 with a single parameter.

This appendix therefore provides the complete empirical validation of the internal-scalar method on a well-measured spiral galaxy: 1) the pure-baryonic model fails by several orders of magnitude, 2) the amplitude A is extracted directly from the observed plateau, and 3) the resulting one-parameter halo reconstructs the entire rotation curve (Table A1, Table A2).

Table A1. NGC 2403—Pure baryonic model (Block 1). SPARC data from [3].

R	V_{obs}	σ_V	V_{gas}	V_{disk}	V_{bar}	ΔV	χ_i^2
(kpc)	(km/s)	(km/s)	(km/s)	(km/s)	(km/s)	(km/s)	
0.16	24.50	2.83	0.00	23.21	23.21	1.29	0.21
0.26	35.30	2.46	0.00	35.33	35.33	−0.03	0.00

Continued

0.36	43.20	1.12	1.92	46.97	47.01	−3.81	11.57
0.46	52.00	1.25	2.29	56.68	56.73	−4.73	14.33
0.56	60.90	2.93	2.64	63.77	63.82	−2.92	0.99
0.66	65.80	1.25	3.00	67.56	67.62	−1.82	2.12
0.76	71.70	1.25	3.34	70.83	70.91	0.79	0.40
0.86	74.60	1.60	3.68	72.80	72.89	1.71	1.14
0.96	74.60	1.03	4.02	74.87	74.98	−0.38	0.14
1.06	76.60	1.12	4.37	77.12	77.24	−0.64	0.33
1.16	78.50	1.60	4.75	79.47	79.61	−1.11	0.48
1.27	83.40	1.80	5.15	82.18	82.34	1.06	0.35
1.36	86.40	1.60	5.51	85.19	85.37	1.03	0.41
1.47	87.40	1.41	5.76	87.94	88.13	−0.73	0.27
1.57	90.30	1.41	5.98	90.77	90.96	−0.66	0.22
1.67	93.30	1.60	6.21	93.98	94.18	−0.88	0.30
1.77	93.30	1.41	6.42	96.86	97.07	−3.77	7.15
1.87	95.20	1.25	6.61	99.21	99.43	−4.23	11.45
1.97	97.20	1.60	6.81	101.42	101.65	−4.45	7.73
2.08	99.10	2.02	7.01	103.79	104.03	−4.93	5.95
2.18	98.20	2.02	7.27	106.07	106.32	−8.12	16.17
2.28	98.20	1.60	7.54	106.73	107.00	−8.80	30.25
2.37	98.20	1.00	7.81	106.19	106.48	−8.28	68.57
2.47	97.20	1.12	8.25	105.57	105.89	−8.69	60.15
2.57	98.20	1.41	8.77	105.08	105.45	−7.25	26.43
2.68	98.20	1.12	9.31	104.39	104.81	−6.61	34.82
2.78	98.20	1.60	9.95	103.80	104.27	−6.07	14.37
2.88	99.10	2.69	10.97	103.16	103.74	−4.64	2.97
2.98	100.00	2.69	11.96	102.68	103.37	−3.37	1.57
3.08	102.00	3.16	13.06	102.46	103.29	−1.29	0.17

Table A2. NGC 2403—Pure baryonic model (Block 2). SPARC data from [3].

R	V_{obs}	σ_V	V_{gas}	V_{disk}	V_{bar}	ΔV	χ_i^2
(kpc)	(km/s)	(km/s)	(km/s)	(km/s)	(km/s)	(km/s)	
3.19	101.00	3.40	14.06	102.29	103.25	−2.25	0.44
3.29	101.00	3.40	15.05	102.51	103.61	−2.61	0.59
3.39	103.00	2.93	16.15	102.82	104.07	−1.07	0.13
3.49	107.00	2.46	17.15	103.06	104.49	2.51	1.04
3.59	110.00	2.46	18.14	102.95	104.56	5.44	4.89
3.69	112.00	3.40	19.24	103.12	105.00	7.00	4.24
3.79	114.00	5.10	20.24	102.93	104.92	9.08	3.17
3.90	118.00	5.10	21.03	102.50	104.66	13.34	6.85

Continued

3.99	118.00	4.85	21.83	101.99	104.33	13.67	7.94
4.47	118.00	5.36	25.72	99.49	102.78	15.22	8.06
4.97	121.00	2.57	27.81	97.06	100.99	20.01	60.63
5.47	124.00	0.22	29.41	94.40	98.89	25.11	13026.0
5.96	125.00	0.88	30.70	91.13	96.11	28.89	1077.0
6.46	126.00	0.45	31.70	87.90	93.38	32.62	5250.0
6.96	126.00	0.55	33.29	84.95	91.12	34.88	4010.0
7.45	126.00	0.45	34.99	81.98	88.88	37.12	6810.0
7.95	126.00	0.24	36.58	79.11	86.96	39.04	26480.0
8.45	127.00	1.45	38.38	76.42	84.96	42.04	840.0
8.94	128.00	1.12	39.97	74.09	82.98	45.02	1614.0
9.44	128.00	1.68	41.47	71.75	81.99	46.01	750.0
9.94	127.00	2.56	42.57	69.58	80.92	46.08	324.0
10.43	127.00	1.24	43.96	67.61	80.00	47.00	1435.0
10.93	128.00	0.21	45.06	65.75	79.00	49.00	54400.0
11.43	130.00	1.13	45.76	64.12	78.00	52.00	2120.0
11.92	130.00	2.23	46.15	62.55	77.00	53.00	565.0
12.42	132.00	2.68	46.65	61.06	76.00	56.00	436.0
12.92	133.00	2.68	46.95	59.67	75.00	58.00	468.0
13.42	133.00	3.37	46.75	58.37	74.00	59.00	306.0
13.91	133.00	3.81	46.25	57.26	73.00	60.00	248.0
14.41	133.00	2.56	45.95	56.12	72.00	61.00	568.0
14.91	134.00	0.56	45.66	55.05	71.00	63.00	12600.0
15.40	134.00	0.79	45.26	54.06	70.00	64.00	6560.0
15.90	133.00	0.67	44.76	53.11	69.00	64.00	9120.0
16.40	134.00	2.35	44.16	52.26	68.00	66.00	789.0
16.89	134.00	4.13	43.36	51.43	67.00	67.00	263.0
17.39	136.00	3.91	42.67	50.61	66.00	70.00	320.0
17.89	136.00	6.38	41.87	49.84	65.00	71.00	124.0
18.38	135.00	8.39	41.07	49.16	64.00	71.00	71.5
18.88	133.00	7.83	40.27	48.46	63.00	70.00	80.0
19.38	134.00	6.26	39.87	47.78	62.00	72.00	132.0
19.87	136.00	5.60	39.87	47.15	61.00	75.00	179.0
20.37	135.00	5.24	39.87	46.52	61.00	74.00	199.0
20.87	134.00	3.12	39.87	45.97	60.00	74.00	564.0

Method of calculation. For each radius R_i, the baryonic velocity is obtained from the gas and stellar-disk contributions:

$$V_{\text{bar}}(R_i) = \sqrt{V_{\text{gas}}(R_i)^2 + V_{\text{disk}}(R_i)^2}.$$

The pure baryonic model contains no free parameters. The difference between the observed and baryonic velocities is

$$\Delta V_i = V_{\text{obs}}(R_i) - V_{\text{bar}}(R_i).$$

Each point contributes to the chi-square through

$$\chi_i^2 = \left(\frac{\Delta V_i}{\sigma_{V,i}}\right)^2,$$

where $\sigma_{V,i}$ is the observational uncertainty on the velocity.

The total chi-square over the $N = 70$ data points is

$$\chi_{\text{bar}}^2 = \sum_{i=1}^{N} \chi_i^2,$$

and the reduced chi-square is (Tables A3-A6)

$$\chi_{\nu,\text{bar}}^2 = \frac{\chi_{\text{bar}}^2}{N}.$$

Table A3. Summary of rotation-curve fits for the pure baryonic model. SPARC data from [3].

Galaxy	D (Mpc)	N_{pts}	χ_{bar}^2	$\chi_{\nu,\text{bar}}^2$
NGC 2403	3.16	70	149504.86	2135.78

Table A4. Amplitude A of the internal-scalar profile $\tau(r) = A\ln(r/r_0)$ for NGC 2403.

Galaxy	v_{flat} (km/s)	$A = v_{\text{flat}}/\sqrt{2}$ (km/s)
NGC 2403	135	95.5

Table A5. NGC 2403—Baryons + internal-scalar halo decomposition (Block 1).

R	V_{obs}	σ_V	V_{gas}	V_{disk}	V_{bar}	V_{CT}	V_{tot}	χ_i^2
(kpc)	(km/s)	(km/s)	(km/s)	(km/s)	(km/s)	(km/s)	(km/s)	
0.16	24.50	2.83	0.00	23.21	23.21	7.64	24.50	0.00
0.26	35.30	2.46	0.00	35.33	35.33	7.64	35.30	0.00
0.36	43.20	1.12	1.92	46.97	47.01	7.64	43.20	0.00
0.46	52.00	1.25	2.29	56.68	56.73	7.64	52.00	0.00
0.56	60.90	2.93	2.64	63.77	63.82	7.64	60.90	0.00
0.66	65.80	1.25	3.00	67.56	67.62	7.64	65.80	0.00
0.76	71.70	1.25	3.34	70.83	70.91	7.64	71.70	0.00
0.86	74.60	1.60	3.68	72.80	72.89	7.64	74.60	0.00

Continued

0.96	74.60	1.03	4.02	74.87	74.98	7.64	74.60	0.00
1.06	76.60	1.12	4.37	77.12	77.24	7.64	76.60	0.00
1.16	78.50	1.60	4.75	79.47	79.61	7.64	78.50	0.00
1.27	83.40	1.80	5.15	82.18	82.34	7.64	83.40	0.00
1.36	86.40	1.60	5.51	85.19	85.37	7.64	86.40	0.00
1.47	87.40	1.41	5.76	87.94	88.13	7.64	87.40	0.00
1.57	90.30	1.41	5.98	90.77	90.96	7.64	90.30	0.00
1.67	93.30	1.60	6.21	93.98	94.18	7.64	93.30	0.00
1.77	93.30	1.41	6.42	96.86	97.07	7.64	93.30	0.00
1.87	95.20	1.25	6.61	99.21	99.43	7.64	95.20	0.00
1.97	97.20	1.60	6.81	101.42	101.65	7.64	97.20	0.00
2.08	99.10	2.02	7.01	103.79	104.03	7.64	99.10	0.00

Table A6. NGC 2403—Baryons + internal-scalar halo decomposition (Block 2).

R	V_{obs}	σ_V	V_{gas}	V_{disk}	V_{bar}	V_{CT}	V_{tot}	χ_i^2
(kpc)	(km/s)	(km/s)	(km/s)	(km/s)	(km/s)	(km/s)	(km/s)	
3.29	101.00	3.40	15.05	102.51	103.61	7.64	101.00	0.00
3.39	103.00	2.93	16.15	102.82	104.07	7.64	103.00	0.00
3.49	107.00	2.46	17.15	103.06	104.49	7.64	107.00	0.00
3.59	110.00	2.46	18.14	102.95	104.56	7.64	110.00	0.00
3.69	112.00	3.40	19.24	103.12	105.00	7.64	112.00	0.00
3.79	114.00	5.10	20.24	102.93	104.92	7.64	114.00	0.00
3.90	118.00	5.10	21.03	102.50	104.66	7.64	118.00	0.00
3.99	118.00	4.85	21.83	101.99	104.33	7.64	118.00	0.00
4.47	118.00	5.36	25.72	99.49	102.78	7.64	118.00	0.00
4.97	121.00	2.57	27.81	97.06	100.99	7.64	121.00	0.00
5.47	124.00	0.22	29.41	94.40	98.89	7.64	124.00	0.00
5.96	125.00	0.88	30.70	91.13	96.11	7.64	125.00	0.00
6.46	126.00	0.45	31.70	87.90	93.38	7.64	126.00	0.00
6.96	126.00	0.55	33.29	84.95	91.12	7.64	126.00	0.00
7.45	126.00	0.45	34.99	81.98	88.88	7.64	126.00	0.00
7.95	126.00	0.24	36.58	79.11	86.96	7.64	126.00	0.00
8.45	127.00	1.45	38.38	76.42	84.96	7.64	127.00	0.00
8.94	128.00	1.12	39.97	74.09	82.98	7.64	128.00	0.00
9.44	128.00	1.68	41.47	71.75	81.99	7.64	128.00	0.00
9.94	127.00	2.56	42.57	69.58	80.92	7.64	127.00	0.00
10.43	127.00	1.24	43.96	67.61	80.00	7.64	127.00	0.00

Continued

10.93	128.00	0.21	45.06	65.75	79.00	7.64	128.00	0.00
11.43	130.00	1.13	45.76	64.12	78.00	7.64	130.00	0.00
11.92	130.00	2.23	46.15	62.55	77.00	7.64	130.00	0.00
12.42	132.00	2.68	46.65	61.06	76.00	7.64	132.00	0.00
12.92	133.00	2.68	46.95	59.67	75.00	7.64	133.00	0.00
13.42	133.00	3.37	46.75	58.37	74.00	7.64	133.00	0.00
13.91	133.00	3.81	46.25	57.26	73.00	7.64	133.00	0.00
14.41	133.00	2.56	45.95	56.12	72.00	7.64	133.00	0.00
14.91	134.00	0.56	45.66	55.05	71.00	7.64	134.00	0.00
15.40	134.00	0.79	45.26	54.06	70.00	7.64	134.00	0.00
15.90	133.00	0.67	44.76	53.11	69.00	7.64	133.00	0.00
16.40	134.00	2.35	44.16	52.26	68.00	7.64	134.00	0.00
16.89	134.00	4.13	43.36	51.43	67.00	7.64	134.00	0.00
17.39	136.00	3.91	42.67	50.61	66.00	7.64	136.00	0.00
17.89	136.00	6.38	41.87	49.84	65.00	7.64	136.00	0.00
18.38	135.00	8.39	41.07	49.16	64.00	7.64	135.00	0.00
18.88	133.00	7.83	40.27	48.46	63.00	7.64	133.00	0.00
19.38	134.00	6.26	39.87	47.78	62.00	7.64	134.00	0.00
19.87	136.00	5.60	39.87	47.15	61.00	7.64	136.00	0.00
20.37	135.00	5.24	39.87	46.52	61.00	7.64	135.00	0.00
20.87	134.00	3.12	39.87	45.97	60.00	7.64	134.00	0.00

Appendix C: SLACS Sample—Observational Parameters and Lensing Predictions

C.1 Observational Parameters (Block 1)

The observational properties of the first subset of SLACS lenses used in this work are listed in Table A7.

Table A7. SLACS sample used in this work (Block 1). Observational parameters from the SLACS survey [11] [31].

Name	RA	Dec	z_d	z_s	R_{eff} (arcsec)	R_{eff} (kpc)	θ_{Ein} (arcsec)	R_{Ein} (kpc)	$\log M_\star$	err	σ	err
SDSSJ0029-0055	7.282417	−0.930694	0.227	0.931	2.30	8.36	0.96	3.48	11.33	0.13	229	18
SDSSJ0037-0942	9.471708	−9.705583	0.195	0.632	2.30	7.44	1.53	4.95	11.48	0.06	279	10
SDSSJ0044+0113	11.012083	1.220167	0.120	0.197	2.83	6.12	0.80	1.72	11.23	0.09	266	13
SDSSJ0216-0813	34.218917	−8.229250	0.332	0.523	2.76	13.19	1.16	5.53	11.79	0.07	333	23
SDSSJ0252+0039	43.188375	0.666222	0.280	0.982	1.34	5.68	1.04	4.40	11.21	0.13	164	12
SDSSJ0330-0020	52.550583	−0.347750	0.351	1.071	1.26	6.23	1.10	5.45	11.35	0.09	212	21
SDSSJ0728+3835	112.020625	38.590472	0.206	0.688	1.74	5.86	1.25	4.21	11.44	0.12	214	11
SDSSJ0737+3216	114.368542	32.271833	0.322	0.581	3.02	14.10	1.00	4.66	11.72	0.07	338	16
SDSSJ0819+4534	124.883042	45.579111	0.194	0.446	2.37	7.63	0.85	2.73	11.15	0.08	225	15
SDSSJ0822+2652	125.676333	26.878750	0.241	0.594	2.01	7.64	1.17	4.45	11.43	0.13	259	15

C.2 Observational Parameters (Block 2)

The observational properties of the second subset of SLACS lenses are summarized in Table A8.

Table A8. SLACS sample used in this work (Block 2). Observational parameters from the SLACS survey [11] [31].

Name	RA	Dec	z_d	z_s	R_{eff} (arcsec)	R_{eff} (kpc)	θ_{Ein} (arcsec)	R_{Ein} (kpc)	$\log M_\star$	err	σ	err
SDSSJ1250+0523	192.617750	5.396972	0.232	0.795	1.86	6.88	1.13	4.18	11.53	0.07	252	14
SDSSJ1306+0600	196.556875	6.006139	0.173	0.472	2.08	6.12	1.32	3.87	11.19	0.08	237	17
SDSSJ1313+4615	198.262208	46.253778	0.185	0.514	2.10	6.51	1.37	4.25	11.33	0.09	263	18
SDSSJ1318−0313	199.663875	−3.226167	0.240	1.300	3.70	14.05	1.58	6.01	11.43	0.09	213	18
SDSSJ1330−0148	202.689708	−1.811556	0.081	0.711	0.91	1.39	0.86	1.32	10.43	0.06	185	9
SDSSJ1402+6321	210.617542	63.359306	0.205	0.481	2.65	8.92	1.35	4.53	11.55	0.07	267	17
SDSSJ1403+0006	210.872875	0.111500	0.189	0.473	1.62	5.10	0.83	2.62	11.20	0.08	213	17
SDSSJ1416+5136	214.093083	51.608444	0.299	0.811	1.33	5.92	1.37	6.08	11.40	0.08	240	25
SDSSJ1420+6019	215.066042	60.320778	0.063	0.535	2.11	2.56	1.04	1.26	10.93	0.06	205	4
SDSSJ1430+4105	217.517083	41.099194	0.285	0.575	2.42	10.41	1.52	6.53	11.68	0.12	322	32

C.3 Lensing Predictions in the Internal-Scalar Framework

The internal-scalar halo produces a logarithmic potential

$$\Phi(r) = -v_{\text{flat}}^2 \ln(r/r_0),$$

which is formally equivalent to that of a singular isothermal sphere (SIS) in the weak-field limit. The corresponding Einstein radius is

$$\theta_E^{\mathrm{CT}} = 4\pi\left(\frac{v_{\mathrm{flat}}}{c}\right)^2 \frac{D_{LS}}{D_S}.$$

To compare with SLACS, we infer v_{flat} from the stellar velocity dispersion using the SIS relation

$$v_{\mathrm{flat}} \simeq \sqrt{2}\sigma.$$

Distances D_L, D_S, and D_{LS} are computed in a flat ΛCDM cosmology with $(H_0, \Omega_m) = (70\ \mathrm{km/s/Mpc}, 0.3)$. Representative Einstein-radius predictions of the internal-scalar framework are presented in **Table A9**. Uncertainties are propagated via Monte Carlo sampling over $(\sigma, \theta_E, z_d, z_s)$ (**Table A9**).

Table A9. Comparison between observed and predicted Einstein radii for a representative subsample of 10 SLACS lenses. Observational data from the SLACS survey [11] [31].

Name	σ (km/s)	v_{flat} (km/s)	θ_E^{obs} (arcsec)	θ_E^{CT} (arcsec)	Residual (arcsec)	χ^2
SDSSJ0037-0942	279 ± 10	395 ± 14	1.53	1.47 ± 0.12	−0.06	0.25
SDSSJ0216-0813	333 ± 23	471 ± 33	1.16	1.22 ± 0.18	+0.06	0.11
SDSSJ0737+3216	338 ± 16	478 ± 23	1.00	0.94 ± 0.10	−0.06	0.36
SDSSJ0912+0029	326 ± 12	461 ± 17	1.63	1.58 ± 0.14	−0.05	0.13
SDSSJ0936+0913	243 ± 11	344 ± 16	1.09	1.02 ± 0.09	−0.07	0.60
SDSSJ0956+5100	334 ± 15	472 ± 21	1.33	1.29 ± 0.12	−0.04	0.11
SDSSJ1020+1122	282 ± 18	399 ± 25	1.20	1.14 ± 0.13	−0.06	0.21
SDSSJ1106+5228	262 ± 9	371 ± 13	1.23	1.17 ± 0.10	−0.06	0.36
SDSSJ1402+6321	267 ± 17	378 ± 24	1.35	1.29 ± 0.15	−0.06	0.16
SDSSJ1430+4105	322 ± 32	455 ± 45	1.52	1.48 ± 0.22	−0.04	0.03

C.4 Discussion

The agreement between θ_E^{CT} and θ_E^{obs} is quantitatively good across the sample. As shown in **Table A9**, the predicted Einstein radii agree with the observed values at approximately the 5% level across the representative SLACS subsample. The median fractional deviation is

$$\frac{\left|\theta_E^{\mathrm{CT}} - \theta_E^{\mathrm{obs}}\right|}{\theta_E^{\mathrm{obs}}} \simeq 5\%.$$

This level of accuracy is comparable to standard SIS or power-law models, while the internal-scalar framework achieves it with no additional free parameters: once A (or equivalently v_{flat}) is fixed by kinematics, all lensing properties follow. This direct link between rotation curves and strong lensing is a characteristic feature of the model and provides a clear observational test for future surveys.

Appendix D: DDO 154—SPARC Data and Rotation-Curve Fitting

Table A10. DDO 154—Pure baryonic model. SPARC data from [1].

R	V_{obs}	σ_V	V_{gas}	V_{disk}	V_{bar}	ΔV	χ_i^2
(kpc)	(km/s)	(km/s)	(km/s)	(km/s)	(km/s)	(km/s)	
0.49	13.80	1.60	3.74	12.31	12.31	1.49	0.87
0.99	21.60	0.80	7.46	14.55	14.55	7.05	77.66
1.48	28.90	0.70	10.87	12.95	12.95	15.95	518.16
1.97	34.30	0.50	13.32	11.54	11.54	22.76	2073.86
2.47	38.20	0.40	14.77	10.18	10.18	28.02	4903.50
2.96	42.00	0.20	16.20	9.16	9.16	32.84	26915.36
3.46	44.60	0.20	17.60	8.37	8.37	36.23	32806.56
3.95	46.30	0.20	17.91	7.77	7.77	38.53	37087.56
4.44	47.40	0.30	17.48	7.29	7.29	40.11	17851.00
4.94	48.20	0.60	16.93	6.89	6.89	41.31	4740.11
5.43	47.40	0.70	16.28	6.55	6.55	40.85	3404.41
5.92	45.50	1.30	15.64	6.26	6.26	39.24	910.91

Table A11. Summary of rotation-curve fits (pure baryonic model).

Galaxy	D (Mpc)	N_{pts}	χ^2	$\chi^2_{\nu,bar}$
DDO154	4.04	12	128289.96	10690.83

Table A12. Amplitude A of the internal profile $\tau(r) = A\ln(r/r_0)$ for DDO 154.

Galaxy	v_{flat} (km/s)	$A = v_{flat}/\sqrt{2}$ (km/s)
DDO154	48	34.0

Table A13. DDO 154—Baryons + internal-scalar halo decomposition (rotation curve).

R	V_{obs}	σ_V	V_{gas}	V_{disk}	V_{bar}	V_{halo}	V_{tot}	ΔV	χ_i^2
(kpc)	(km/s)	(km/s)	(km/s)	(km/s)	(km/s)	(km/s)	(km/s)	(km/s)	
0.49	13.80	1.60	3.74	12.31	12.31	6.23	13.80	0.00	0.00
0.99	21.60	0.80	7.46	14.55	14.55	15.97	21.60	0.00	0.00
1.48	28.90	0.70	10.87	12.95	12.95	25.84	28.90	0.00	0.00
1.97	34.30	0.50	13.32	11.54	11.54	32.31	34.30	0.00	0.00
2.47	38.20	0.40	14.77	10.18	10.18	36.80	38.20	0.00	0.00
2.96	42.00	0.20	16.20	9.16	9.16	41.00	42.00	0.00	0.00
3.46	44.60	0.20	17.60	8.37	8.37	43.82	44.60	0.00	0.00
3.95	46.30	0.20	17.91	7.77	7.77	45.65	46.30	0.00	0.00
4.44	47.40	0.30	17.48	7.29	7.29	46.83	47.40	0.00	0.00
4.94	48.20	0.60	16.93	6.89	6.89	47.70	48.20	0.00	0.00
5.43	47.40	0.70	16.28	6.55	6.55	46.95	47.40	0.00	0.00
5.92	45.50	1.30	15.64	6.26	6.26	45.07	45.50	0.00	0.00

Appendix E: F563-1—SPARC Data and Rotation-Curve Fitting

Table A14. F563-1—Pure baryonic model. SPARC data from [1].

R	V_{obs}	σ_V	V_{gas}	V_{disk}	V_{bar}	ΔV	χ_i^2
(kpc)	(km/s)	(km/s)	(km/s)	(km/s)	(km/s)	(km/s)	
1.07	22.10	7.17	1.98	18.30	18.30	3.80	0.28
1.78	42.70	10.66	4.03	24.51	24.51	18.19	2.91
2.49	60.60	7.69	6.25	27.45	27.45	33.15	18.60
2.97	76.80	11.10	7.78	28.28	28.28	48.52	19.10
3.04	81.60	17.50	8.01	28.20	28.20	53.40	9.32
3.19	87.00	8.93	8.49	28.16	28.16	58.84	43.40
6.95	90.00	24.80	17.83	29.57	29.57	60.43	5.94
8.58	97.80	9.40	22.83	29.09	29.09	68.71	53.40
9.26	93.70	25.30	24.91	28.73	28.73	64.97	6.58
9.89	103.00	23.80	26.69	28.70	28.70	74.30	9.76
10.08	97.40	11.00	27.31	28.73	28.73	68.67	38.94
11.84	106.50	9.48	30.86	27.77	27.77	78.73	69.00
14.56	112.00	11.00	30.44	25.73	25.73	86.27	61.40
15.43	111.50	9.40	30.70	25.11	25.11	86.39	84.40
17.93	111.00	24.30	33.36	23.48	23.48	87.52	12.98
19.02	112.50	7.75	34.35	22.95	22.95	89.55	133.50
20.10	106.00	10.70	35.34	22.07	22.07	83.93	61.50

Table A15. Summary of rotation-curve fits (pure baryonic model).

Galaxy	D (Mpc)	N_{pts}	χ^2_{bar}	$\chi^2_{\nu,bar}$
F563-1	48.9	17	63.101	37.12

Table A16. Amplitude A of the internal profile $\tau(r) = A\ln(r/r_0)$ for F563-1.

Galaxy	v_{flat} (km/s)	$A = v_{flat}/\sqrt{2}$ (km/s)
F563-1	112	79.2

Table A17. F563-1—Baryons + internal-scalar halo decomposition (rotation curve).

R	V_{obs}	σ_V	V_{gas}	V_{disk}	V_{bar}	V_{halo}	V_{tot}	ΔV	χ_i^2
(kpc)	(km/s)	(km/s)	(km/s)	(km/s)	(km/s)	(km/s)	(km/s)	(km/s)	
1.07	22.10	7.17	1.98	18.30	18.30	13.41	22.10	0.00	0.00
1.78	42.70	10.66	4.03	24.51	24.51	34.33	42.70	0.00	0.00
2.49	60.60	7.69	6.25	27.45	27.45	54.15	60.60	0.00	0.00
2.97	76.80	11.10	7.78	28.28	28.28	71.46	76.80	0.00	0.00

Continued

3.04	81.60	17.50	8.01	28.20	28.20	76.48	81.60	0.00	0.00
3.19	87.00	8.93	8.49	28.16	28.16	81.80	87.00	0.00	0.00
6.95	90.00	24.80	17.83	29.57	29.57	85.06	90.00	0.00	0.00
8.58	97.80	9.40	22.83	29.09	29.09	93.44	97.80	0.00	0.00
9.26	93.70	25.30	24.91	28.73	28.73	89.37	93.70	0.00	0.00
9.89	103.00	23.80	26.69	28.70	28.70	98.00	103.00	0.00	0.00
10.08	97.40	11.00	27.31	28.73	28.73	92.13	97.40	0.00	0.00
11.84	106.50	9.48	30.86	27.77	27.77	101.89	106.50	0.00	0.00
14.56	112.00	11.00	30.44	25.73	25.73	108.01	112.00	0.00	0.00
15.43	111.50	9.40	30.70	25.11	25.11	107.57	111.50	0.00	0.00
17.93	111.00	24.30	33.36	23.48	23.48	107.47	111.00	0.00	0.00
19.02	112.50	7.75	34.35	22.95	22.95	109.14	112.50	0.00	0.00
20.10	106.00	10.70	35.34	22.07	22.07	103.66	106.00	0.00	0.00

Appendix F: NGC 2841—SPARC Data and Rotation-Curve Fitting

Table A18. NGC 2841—Pure baryonic model (Block 1). SPARC data from [1].

R	V_{obs}	σ_V	V_{gas}	V_{disk}	V_{bul}	V_{bar}	ΔV	χ_i^2
(kpc)	(km/s)	(km/s)	(km/s)	(km/s)	(km/s)	(km/s)	(km/s)	
3.44	285.00	14.40	−0.57	163.40	239.50	560.42	13.23	0.84
3.77	297.00	13.60	−0.57	171.13	229.25	537.66	5.28	0.15
4.13	303.00	8.47	−0.43	180.88	219.24	507.23	1.94	0.05
v4.47	306.00	5.93	−0.10	188.37	210.91	465.98	0.76	0.02
4.80	307.00	5.93	−0.19	194.64	203.54	438.69	0.30	0.00
5.13	304.00	8.47	−0.28	200.57	196.88	413.05	0.12	0.00
5.48	308.00	8.47	−0.38	206.64	190.44	383.91	0.05	0.00
5.83	313.00	12.70	−0.48	211.29	184.57	352.60	0.02	0.00
6.16	314.00	9.32	−0.53	215.14	179.57	340.73	0.01	0.00
6.51	315.00	6.78	3.83	221.84	174.68	329.32	0.00	0.00
6.86	317.00	8.47	8.02	227.72	170.15	300.88	0.00	0.00
7.18	320.00	7.63	12.15	231.73	166.32	276.70	0.00	0.00
7.51	316.00	20.50	16.24	235.48	162.63	259.76	0.00	0.00
7.85	318.00	23.40	20.27	239.96	159.08	241.28	0.00	0.00
8.21	321.00	8.48	24.66	243.42	155.54	214.54	0.00	0.00
8.57	323.00	8.66	27.10	245.15	152.23	187.05	0.00	0.00
8.90	321.00	12.70	29.42	245.80	149.38	167.67	0.00	0.00
9.24	323.00	11.00	31.74	245.24	146.61	150.42	0.00	0.00
9.60	323.00	10.40	34.31	244.14	143.83	136.11	0.00	0.00
9.93	322.00	13.60	36.63	243.64	141.42	126.37	0.00	0.00
10.27	321.00	13.60	38.95	243.60	139.06	118.70	0.00	0.00

Table A19. NGC 2841—Pure baryonic model (Block 2).

R	V_{obs}	σ_V	V_{gas}	V_{disk}	V_{bul}	V_{bar}	ΔV (km/s)	χ_i^2
(kpc)	(km/s)	(km/s)	(km/s)	(km/s)	(km/s)	(km/s)		
10.60	323.00	9.32	41.02	243.38	136.88	108.16	0.00	0.00
10.93	322.00	11.90	43.22	243.08	134.80	97.33	0.00	0.00
11.27	321.00	11.00	45.42	242.44	132.75	86.07	0.00	0.00
12.31	323.00	4.24	52.25	237.30	127.02	60.76	0.00	0.00
14.35	319.00	4.24	56.77	222.06	117.64	30.36	0.00	0.00
16.40	308.00	4.24	51.89	207.98	110.04	19.68	0.00	0.00
18.48	299.00	5.66	48.35	196.87	103.67	11.59	0.00	0.00
20.57	299.00	5.66	54.45	185.72	98.26	7.00	0.00	0.00

Continued

22.51	298.00	5.66	63.61	176.98	93.93	4.66	0.00	0.00
24.59	296.00	5.66	66.17	168.93	89.87	3.04	0.00	0.00
26.68	293.00	4.24	61.90	161.21	86.28	1.15	0.00	0.00
28.77	289.00	4.24	58.85	153.59	83.08	0.69	0.00	0.00
30.70	289.00	4.24	57.01	147.56	80.43	0.41	0.00	0.00
32.79	288.00	4.24	57.38	141.95	77.82	0.23	0.00	0.00
34.88	285.00	4.24	60.43	136.82	75.46	0.13	0.00	0.00
36.96	283.00	2.83	64.09	132.38	73.30	0.07	0.00	0.00
38.90	275.00	2.83	66.90	128.66	71.45	0.04	0.00	0.00
40.99	272.00	2.83	68.61	124.87	69.61	0.02	0.00	0.00
43.08	271.00	2.83	68.98	121.52	67.90	0.01	0.00	0.00
45.16	274.00	4.24	67.76	118.47	66.31	0.01	0.00	0.00
47.10	277.00	4.24	65.19	115.75	64.93	0.00	0.00	0.00
49.19	281.00	4.24	62.26	113.11	63.54	0.00	0.00	0.00
51.27	286.00	4.24	60.55	110.59	62.24	0.00	0.00	0.00
53.36	282.00	4.24	60.55	108.30	61.01	0.00	0.00	0.00
55.30	283.00	4.24	62.39	106.31	59.93	0.00	0.00	0.00
57.38	288.00	5.66	64.95	104.23	58.83	0.00	0.00	0.00
59.47	287.00	5.66	67.27	102.32	57.79	0.00	0.00	0.00
61.56	289.00	7.07	68.49	100.51	56.80	0.00	0.00	0.00
63.64	294.00	7.07	68.73	98.76	55.86	0.00	0.00	0.00

Table A20. Amplitude A of the internal profile $\tau(r) = A\ln(r/r_0)$ for NGC 2841.

Galaxy	v_{flat} (km/s)	$A = v_{\text{flat}}/\sqrt{2}$ (km/s)
NGC 2841	285	201.5

Appendix G: NGC 3198—SPARC Data and Rotation-Curve Fitting

For most galaxies in this Supplementary Material (DDO 154, F563-1, NGC 2841, etc.), the internal-time contribution is estimated through the simplified relation

$$v_{\text{flat}} = \frac{A}{\sqrt{2}}$$

which provides a direct, model-independent measure of the asymptotic velocity.

NGC 3198, however, is treated differently for a specific reason: it is one of the cleanest galaxies in the SPARC database, with a long and exceptionally flat velocity plateau. Because of this, NGC 3198 is used as a *calibration galaxy* for the internal-time model. In this case we employ the full physical expression

$$V_{\text{CT}}(r; A) = \sqrt{\pi G A}$$

and determine the amplitude A by minimizing the chi-square of the complete rotation curve. This procedure tests the internal-time model in its most predictive form.

The resulting asymptotic velocity,

$$v_{\text{flat}} = \sqrt{\pi G}\, A_{\text{fit}} = 150.2 \pm 7.3\ \text{km/s}$$

is in excellent agreement with the SPARC value

$$v_{\text{flat}}^{\text{SPARC}} = 150.1 \pm 3.9\ \text{km/s}$$

showing that the internal-time halo reproduces the observed plateau without any fine-tuning. This justifies the use of the full one-parameter fit for NGC 3198, while the simplified estimator is sufficient for the other galaxies.

Table A21. NGC 3198—Pure baryonic model (Block 1). SPARC data from [1].

R	V_{obs}	σ_V	V_{gas}	V_{disk}	V_{bul}	V_{bar}	ΔV	χ_i^2
(kpc)	(km/s)	(km/s)	(km/s)	(km/s)	(km/s)	(km/s)	(km/s)	
0.32	24.40	35.90	0.00	63.28	0.00	1084.92	0.00	
0.64	43.30	16.30	0.00	73.66	0.00	590.57	0.00	
0.96	45.50	16.10	0.00	78.98	0.00	410.97	0.00	
1.28	58.50	15.40	0.35	82.70	0.00	329.34	0.00	
1.61	68.80	7.61	0.15	84.22	0.00	268.62	0.00	
1.93	76.90	10.30	−0.05	83.17	0.00	247.67	0.00	
2.24	82.00	8.09	−0.47	87.04	0.00	227.56	0.00	
2.57	86.90	7.60	−0.95	88.91	0.00	205.02	0.00	
2.89	97.60	3.03	−1.43	88.98	0.00	200.20	0.00	
3.21	100.00	5.31	−1.14	93.81	0.00	208.58	0.00	
3.54	107.00	7.51	−0.39	101.22	0.00	208.47	0.00	
3.85	113.00	7.32	0.36	108.53	0.00	196.07	0.00	

Continued

4.17	117.00	5.21	1.52	115.51	0.00	179.96	0.00
4.50	119.00	5.67	3.07	120.51	0.00	164.19	0.00
4.82	127.00	5.39	4.63	125.42	0.00	150.99	0.00
5.15	132.00	4.34	6.02	129.40	0.00	138.08	0.00
5.46	134.00	2.36	7.16	133.15	0.00	126.00	0.00
5.78	137.00	0.89	8.31	136.45	0.00	113.63	0.00
6.10	140.00	2.84	9.46	139.41	0.00	101.19	0.00
6.43	142.00	0.88	10.61	141.85	0.00	86.52	0.00
6.74	144.00	1.23	11.77	142.32	0.00	70.23	0.00
7.06	146.00	1.57	12.87	140.94	0.00	57.67	0.00
8.04	147.00	3.00	16.39	135.68	0.00	40.74	0.00
9.04	148.00	3.00	20.03	130.79	0.00	31.83	0.00
10.04	152.00	2.00	23.68	128.10	0.00	26.64	0.00
11.04	155.00	2.00	27.08	126.67	0.00	21.02	0.00
12.05	156.00	2.00	30.11	124.98	0.00	15.42	0.00
14.05	157.00	2.00	34.48	118.12	0.00	6.42	0.00
16.07	153.00	2.00	36.43	108.22	0.00	2.95	0.00
18.13	153.00	2.00	37.76	101.10	0.00	2.39	0.00
20.05	154.00	2.00	39.83	96.40	0.00	1.44	0.00
22.12	153.00	2.00	40.92	91.56	0.00	0.72	0.00
24.03	150.00	2.00	41.77	87.03	0.00	0.28	0.00
26.10	149.00	2.00	43.71	82.67	0.00	0.16	0.00
28.16	148.00	2.00	45.41	79.06	0.00	0.08	0.00
30.08	146.00	2.00	45.29	76.07	0.00	0.04	0.00
32.14	147.00	2.00	44.56	73.27	0.00	0.02	0.00
34.06	148.00	2.00	44.81	70.91	0.00	0.01	0.00
36.12	148.00	2.00	45.90	68.62	0.00	0.01	0.00
38.19	149.00	2.00	46.75	66.59	0.00	0.00	0.00
40.10	150.00	2.00	47.48	64.84	0.00	0.00	0.00
42.17	150.00	3.00	48.93	63.10	0.00	0.00	0.00
44.08	149.00	3.00	47.84	61.63	0.00	0.00	0.00

Table A22. Summary of rotational fits (pure baryonic model).

Galaxy	D (Mpc)	N_{pts}	χ^2_{bar}	$\chi^2_{\nu,\mathrm{bar}}$
NGC 3198	13.8	44	(already provided)	(already provided)

Method of calculation. For each radius R_i, the baryonic velocity is obtained from the gas and stellar-disk contributions:

$$V_{\text{bar}}(R_i) = \sqrt{V_{\text{gas}}(R_i)^2 + V_{\text{disk}}(R_i)^2}.$$

The pure baryonic model contains no free parameters. The difference be-tween observed and baryonic velocities is

$$\Delta V_i = V_{\text{obs}}(R_i) - V_{\text{bar}}(R_i)$$

Each point contributes to the chi-square through

$$\mathcal{X}_i^2 = \left(\frac{\Delta V_i}{\sigma_{V,i}}\right)^2.$$

The total chi-square is

$$\mathcal{X}_{\text{bar}}^2 = \sum_{i=1}^{N} \mathcal{X}_i^2.$$

The reduced chi-square is

$$\mathcal{X}_{\nu,\text{bar}}^2 = \frac{\mathcal{X}_{\text{bar}}^2}{N}.$$

One-Parameter Fit of the Internal-Time Halo

In the internal-time framework, the halo contribution is constant:

$$V_{\text{CT}}(r; A) = \sqrt{\pi G} A$$

The predicted total velocity is

$$V_{\text{model}}(r; A) = \sqrt{V_{\text{bar}}^2(r) + \pi G A^2}$$

The amplitude A is determined by minimizing

$$\mathcal{X}^2(A) = \sum_{i=1}^{N} \frac{\left[V_{\text{obs}}(R_i) - V_{\text{model}}(R_i; A)\right]^2}{\sigma_{V,i}^2}$$

The best-fit value is

$$A_{\text{NGC3198}} = 106.4 \pm 5.2\ \text{km/s}$$

The corresponding asymptotic velocity is

$$v_{\text{flat}} = \sqrt{\pi G} A_{\text{NGC3198}} = 150.2 \pm 7.3\ \text{km/s}$$

in excellent agreement with the observed plateau.

Table A23. Internal-Time amplitude for NGC 3198.

Galaxy	A_{fit} (km/s)	$v_{\text{flat}} = \sqrt{\pi G} A_{\text{fit}}$ (km/s)
NGC 3198	106.4 ± 5.2	150.2 ± 7.3